SANDIA REPORT SAND80-2627 • Unlimited Release • UC-80
Printed November 1981

Modeling Turbine-Missile Impacts Using the HONDO Finite Element Code

Karl W. Schuler

Prepared by
Sandia National Laboratories
Albuquerque, New Mexico 87185 and Livermore, California 94550
for the United States Department of Energy
under Contract DE-AC04-76DP00789

This work was performed for Electric Power Research Institute (EPRI) under
Contract No. E(29-2)-3568/RP399-1

Issued by Sandia National Laboratories, operated for the United States Department of Energy by Sandia Corporation.

Printed in the United States of America
Available from
National Technical Information Service
U.S. Department of Commerce
5285 Port Royal Road
Springfield, VA 22161

NTIS price codes
Printed copy: $ 7.00
Microfiche copy: A01

SAND--80-2627

DE82 006875

SAND80-2627

MODELING TURBINE-MISSILE IMPACTS USING THE HONDO FINITE-ELEMENT CODE*

K. W. Schuler
Division 5522

Sandia National Laboratories**
Albuquerque, New Mexico 87185

Prepared for
Electric Power Research Institute
3412 Hillview Avenue
Palo Alto, California

EPRI Project Manager:
George E. Sliter

Abstract

Calculations have been performed using the dynamic finite element code HONDO to simulate a full scale rocket sled test. In the test a rocket sled was used to launch at a velocity of 150 m/s (490 ft/s), a 1527 kg (3366 lb) fragment of a steam turbine rotor disk into a structure which was a simplified model of a steam turbine casing. In the calculations the material behavior of and boundary conditions on the target structure were varied to assess its energy absorbing characteristics. Comparisons are made between the calculations and observations of missile velocity and strain histories of various points of the target structure.

---

* This work was performed for Electric Power Research Institute (EPRI) under Contract No. E(29-2)-3568/RP399-1.

** A U. S. Department of Energy Facility.

TABLE OF CONTENTS

I. Introduction

In the design of nuclear power plants adequate protection must be provided against internally generated missiles. The International Atomic Energy Agency (IAEA) safety guide on this subject discusses [1] various internal missile sources which must be considered. Of particular interest here are the rotating parts of the plant's main turbine generator which can attain considerable energy. In the event of failure this energy can be converted into translational kinetic energy of rotor fragments. In assessing the effects of these fragments the IAEA concludes that "since rotating machinery usually involves a heavy stationary structure surrounding the rotating parts, some consideration may be given to energy loss after failure due to the energy-absorbing characteristics of the stationary parts." In this paper we employ a structural analysis finite element program, HONDO [2] to evaluate the energy absorbing characteristics of a structure which is an idealization of the complex structure surrounding an actual turbine rotor.

HONDO is a finite element computer code which was developed for use in the analysis of large deformation, inelastic, dynamic response of structures such as that encountered in severe accidents. For this reason, the HONDO

code is well suited for use in the analysis of the impact between a turbine missile fragment and the surrounding stationary structure. This report is a description of how HONDO was used to simulate the blunt impact, turbine missile, sled track test [3]. In this test, a rocket sled accelerated a turbine segment to 490 ft/sec (150 m/s) and projected the segment into two semi-circular rings which simulated the stator support and shroud of a steam turbine. The majority of this report will detail the results of a baseline calculation which was also obtained by other investigators using different computer codes, e.g. [4].

In the baseline calculation only the impact of the missile with the first ring is considered. The material of the ring is assumed to be a rate-dependent elastic-plastic material with multi-linear hardening. The ends of the ring are assumed to be rigidly fixed throughout the calculation. The incorporation of this material model, as well as the requirements of computing some non-standard output quantities, required minor modifications to HONDO. These modifications will be described in subsequent sections.

A calculation which had the same boundary conditions and material hardening behavior, but in which the ring material was rate independent, was performed for comparison with the baseline calculations.

The results of the baseline and the rate-independent calculations predicted larger turbine missile decelerations

than those measured in the experiment. For this reason, a third calculation was performed which incorporated free-end conditions on the ring. This calculation indicated that in the first few milliseconds, the missile slows down at a rate similar to that of the baseline calculations; however, at later times (3-9 ms after impact), the predicted acceleration more closely matches that measured in the experiment.

It should be emphasized that all of these calculations were completed without extensive modifications to HONDO. The modifications which were made were only to simplify the interpretation and printing of the output and to incorporate a particular material model in the code.

II. Baseline Calculation

The problem geometry, boundary conditions, and material models for the baseline calculations were outlined by Sliter [5, 6]. The experimental arrangement is shown schematically in Figure 1a. In the experiment, a non-rotating turbine segment impacted the casing in a blunt but off-center orientation (Figure 1a) at a velocity of 490 ft/sec (150 m/s). The undeformed mesh which was used in the calculations is shown in Figure 2. In the baseline and rate-independent calculation, fixed-end boundary conditions were applied to the nodes along lines A-A and B-B. The boundary conditions employed for the free end calculations were sliding interfaces along lines CC and DD. Four elements were used through the radial thickness of the

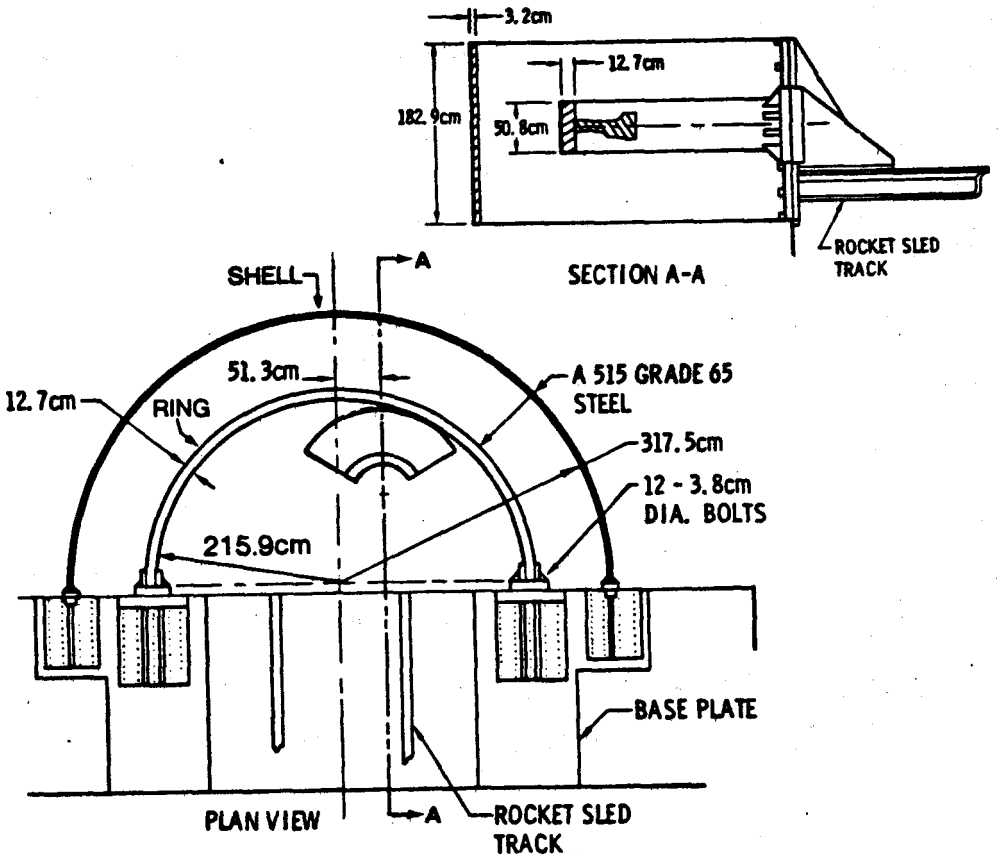

Fig. 1a Plan View and Section of Experimental Arrangement. The initial line of flight of the turbine segment center of mass is along the section line AA.

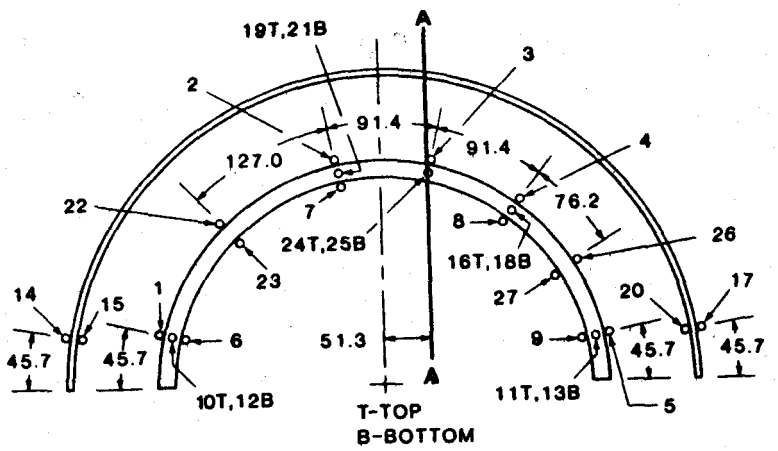

Fig. 1b Schematic of Ring and Shell Showing Strain Gage Locations All dimensions are in centimeters. The initial line of flight of the turbine segment center of mass is along the line AA 51.3 cm to the right of the ring centerline.

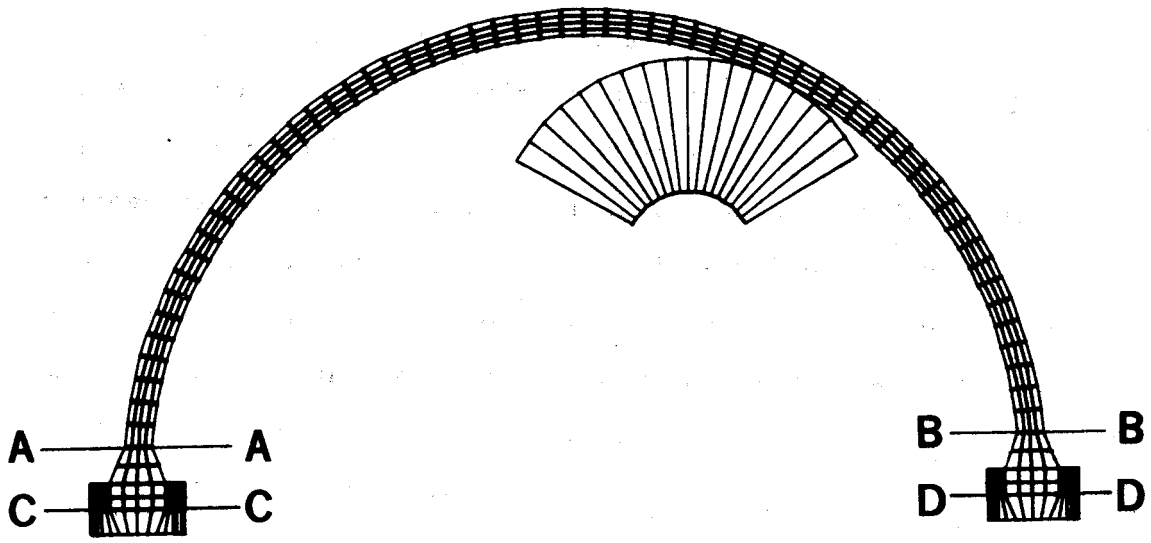

Figure 2. Undeformed Mesh Geometry

ring. In some early calculations, only two elements were employed through the thickness. The difference between these two representations was minor as far as displacements and velocities were concerned. Four elements were used in later calculations because it was felt they would provide better estimates of strains without causing a significant increase in computational times.

Section A-A of Figure 1a shows that the ring had a rectangular cross section 12.7 cm thick by 20" (50.8 cm) high and the turbine segment had a very complicated cross section with a height of 6.1" (15.5 cm) along the impacting edge. In the calculation, the missile was assumed to be 20" (50.8 cm) high and its density was adjusted to provide the same total mass as the actual missile. With this assumption both the ring and the missile have the same height. Since both the top and bottom surfaces of the ring and missile are stress free, it is reasonable to assume that stresses in the vertical direction are identically zero and to perform the calculations using a plane stress approxmiation with a sliding interface incorporated between the turbine missile and ring.

This treatment of the turbine missile means that any bending of the cross section of the ring out of the plane of the calculations is neglected. In examining the post-test deformation of the ring, it was observed that out-of-plane deformation of the ring had occurred around the center of contact with the edge of the missile. In the center of this contact area, the middle of the ring was displaced outward

by about 1-5/8" (4.1 cm) relative to the top and bottom edges. The amount of energy absorbed in this out-of-plane bending can be estimated based on the assumption that a perfectly plastic hinge forms at the center of the ring along the line of contact with the edge of the turbine missile. Assuming a 40,000 psi (276 MPa) yield strength for the ring material and an 80" (2m) length for the plastic hinge an energy dissipation of about 3×10^6 ft-lbs (0.3MJ) could be attributed to this out of plane bending. Since this is only about 2% of the initial kinetic energy of the missile, neglect of this out of plane motion appears justifiable.

A final consideration with regard to the sliding interface is the specification of the interface modulus and friction coefficient. The sliding interface routine in HONDO checks for interference between the nodes on each side of the interface. If interference is present, a force is applied to the nodes. This force is determined by the amount of interference and user-supplied interface modulus. This force procedure does not guarantee that displacements and, hence, velocities at the interface will be treated correctly. To investigate the sensitivity to changes in interface modulus, a number of calculations were performed in which the modulus was varied from 30×10^4 to 30×10^8 psi (2 to 2×10^4 GPa). It was found that an interface modulus which was in the range 30×10^6 to 30×10^7 psi (2×10^2 to 2×10^3 GPa), gave the "best results."

"Best results" means that the nodes on the interface did not undergo a significant amount of penetration nor did large gaps form along the interface.

When the fixed-end constraints on the ring were removed in the free-end calculation, a large gap opened at late times at the center of the contact area. The formation of this gap was associated with sliding between the ring and missile. Increasing or decreasing the interface modulus did not improve this situation and it was found necessary to incorporate friction at the interface to prevent relative sliding between the ring and the turbine missile. Since this inclusion of friction results in a more realistic interface condition, it was incorporated in all the results reported here.

The behavior of the A515 mild steel from which the ring was fabricated was modeled as a rate-dependent elastic-plastic material with a multi-linear isotropic hardening curve. Figure 3 shows the quasi-static stress-strain curve of this material along with the piecewise linear fit prescribed by Sliter [6]. The elastic-plastic constitutive equation available in HONDO was modified to include this piecewise linear fit. Results of a HONDO calculation in which a single element simulated a quasi-statically loaded test specimen is also shown on this figure verifying that the modified constitutive equation was indeed calculating the correct stress-strain behavior. The rate dependence followed the equation specified in Reference [6].

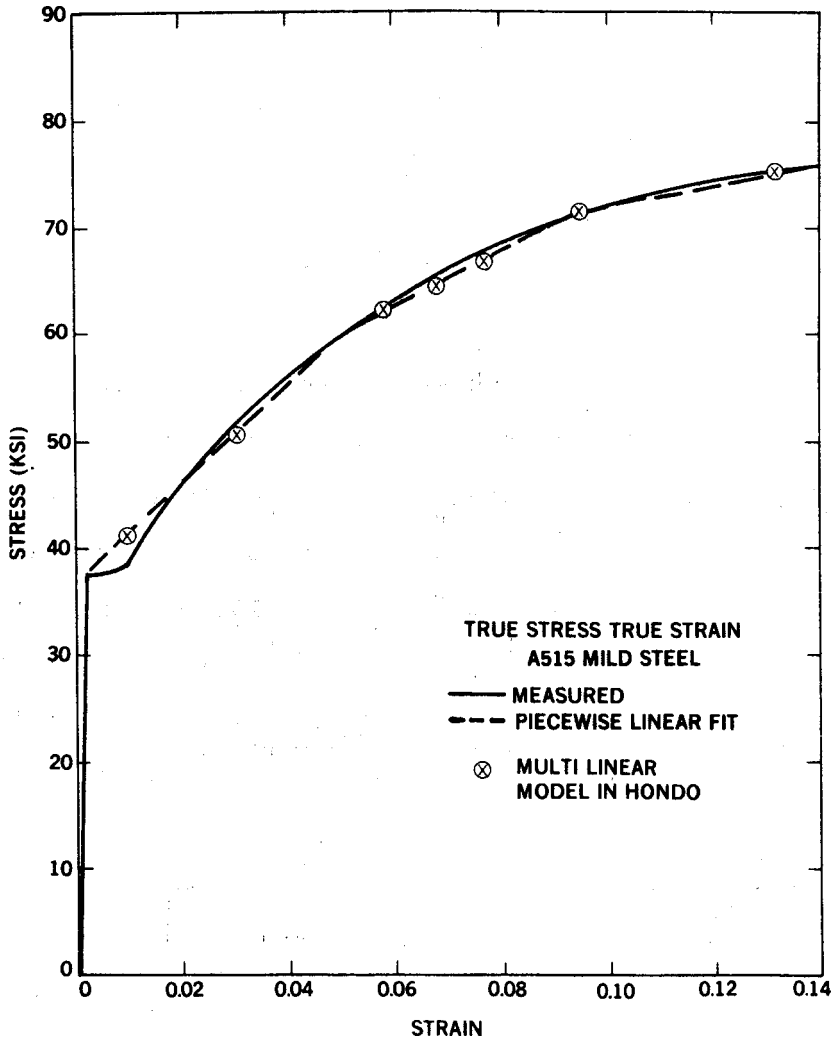

Figure 3. Stress Strain Curve for A515 Mild Steel

$$\frac{\sigma_D}{\sigma_O} = 1 + \left(\frac{\dot{\varepsilon}}{40.4}\right)^{1/5}$$

where σ_D is the dynamic stress, σ_O the value from the static stress-strain curve, and $\dot{\varepsilon}$ is the strain-rate. In conjunction with this study, material testing was carried out by L. Costin of Sandia National Laboratories to provide high-rate loading data for this steel. A detailed discussion of his tests, results and recommendations can be found in the Appendix.

The turbine missile was modeled as a linearly elastic material having properties of steel and an extremely large yield stress. Thus, it is deformable; however, the maximum deformation of the turbine segment is very small and it is essentially a rigid body. One calculation was performed in which the modulus of the turbine segment was increased by a factor of 10; however, this caused the calculational time to increase commensurately. Since the deformation of the segment is small, it was not believed necessary to incorporate greater rigidity into the missile.

Determination of the linear and angular momentum, the translational velocity, and the energy of the turbine segment are, of course, of prime concern in the turbine missile problem. Since these quantities are not normally computed by HONDO, an additional output routine was coded to provide translational velocities, C. G. location, angular velocity, and kinetic energy of the missile.

In the sled track test, strain gages were bonded to the ring at locations shown in Figure 1b. In order to make comparisons with these experimental data, a special strain calculation was incorporated in the analysis. The engineering strain ε, at a given gage location was calculated by

$$\varepsilon = \frac{\ell - \ell_o}{\ell_o}$$

where:

$$\ell = [(R(I) - R(J))^2 + (Z(I)-Z(J))^2]^{1/2}$$

$$\ell_o = [R_o(I) - R_o(J))^2 + (Z_o(I) - Z_o(J))^2]^{1/2}$$

and I and J are the node numbers adjacent to the strain gage location.

III. Baseline Calculational Results

To facilitate comparisons between the various investigators, Sliter [7] requested that nine plots of the calculational results be prepared at specific scales. These plots are presented and discussed in this section.

The deformed shape of the ring middle surface at 3.3 ms after impact is shown in Figure 4. At this time, we note that there is little bending deformation of the ring near the support and that at point B, the bending of the ring has tended to flatten it out. At 9.0 ms after impact, the deformed ring shape shown in Figure 5 indicates that

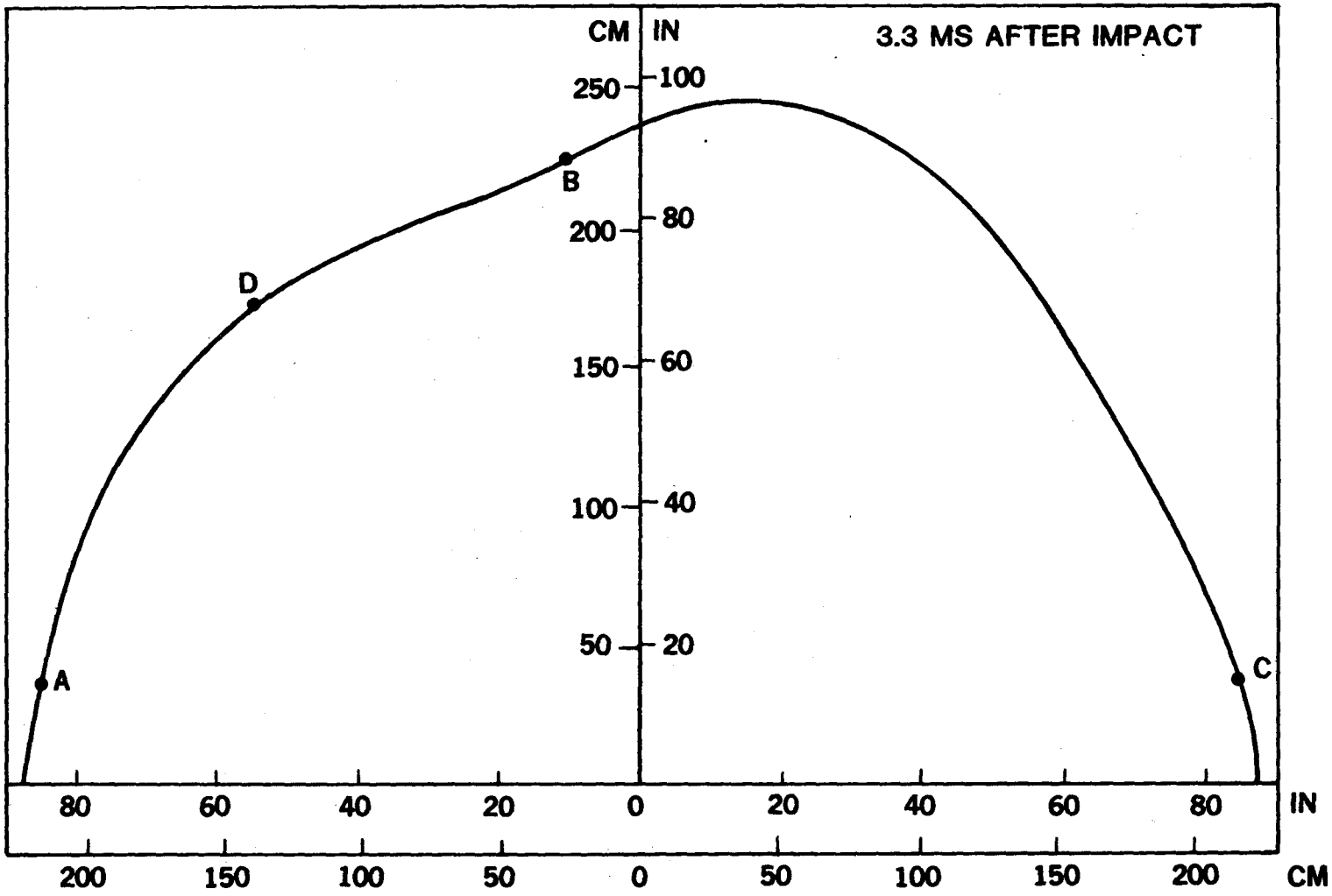

Figure 4. Deformation of Ring Midsurface 3.3 ms After Impact

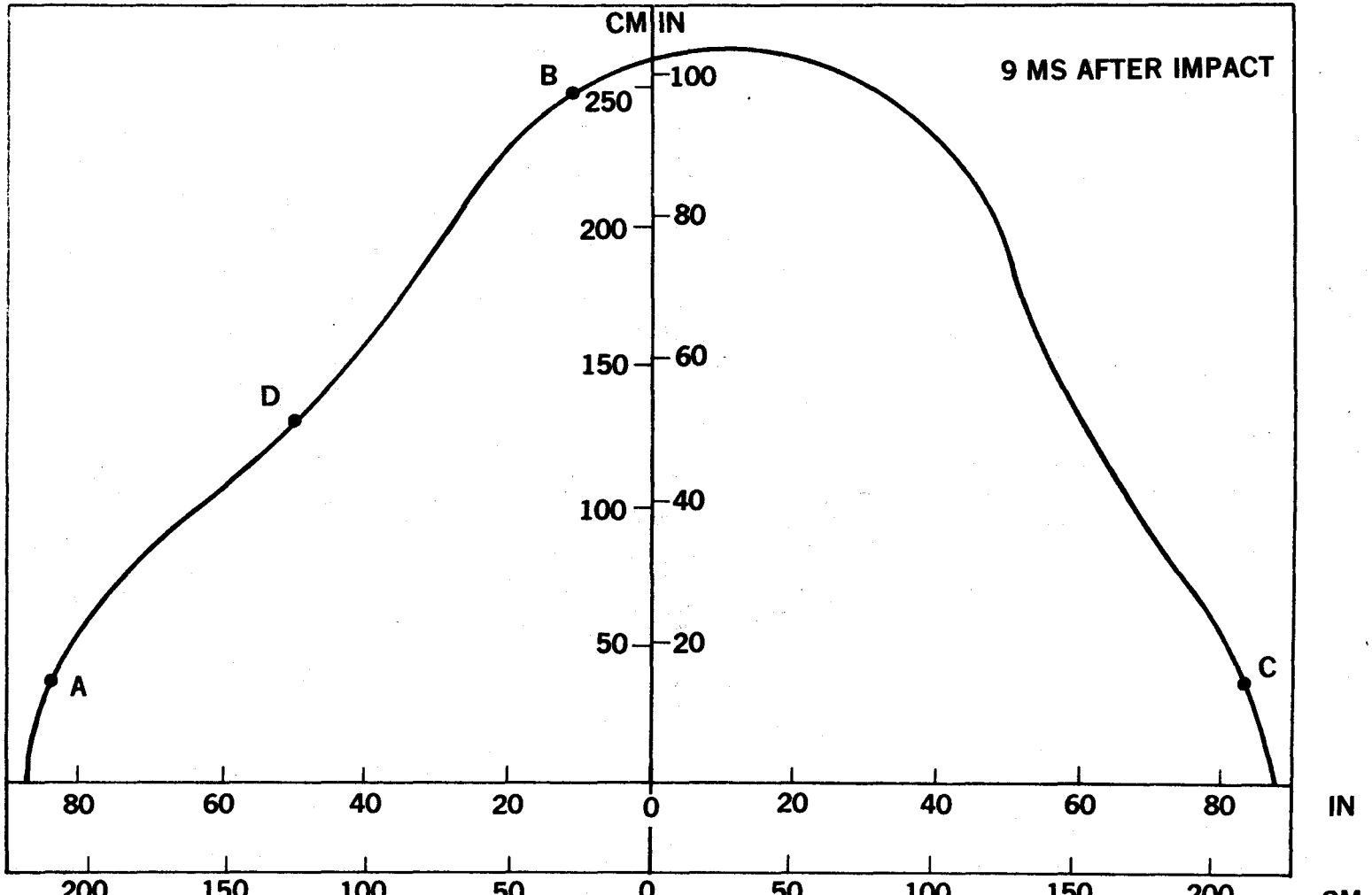

Figure 5. Deformation of Ring Midsurface 9.0 ms After Impact

significant bending has occurred near both support points A and C, and instead of the curvature at point B flattening out, it has become a tighter radius of curvature as the ring attempts to conform to the outer radius of the turbine segment.

Figure 6 shows the displacement history, both transverse and along the line of flight of the missile, of a point on the ring which initially is located on the middle surface 59.7 (1.5m) along circumference to the left of the ring centerline. This point is denoted by point D on Figures 4 and 5.

Turning now to the motion of the turbine segment, Figure 7 shows the line-of-flight displacement of the missile segment's center of mass. Figure 8 shows the velocity of the center of mass in the direction of the line of flight. We note that at 9 ms, the turbine segment has virtually stopped. In the experiment, both the turbine segment and ring were observed to be moving at a velocity of approximately 135 ft/sec (41 m/s) at this time.

Figure 9 shows how the balance between strain and kinetic energy changes with time. During the first 3 ms, the decrease in the kinetic energy of the missile appears both as kinetic and strain energy of ring. After this time, the restraints provided by the fixed ends of the ring slow it down and decrease its kinetic energy. Throughout the calculation, the sum of the kinetic and strain energy should remain constant. At 9 ms, the sum is within 4% of the

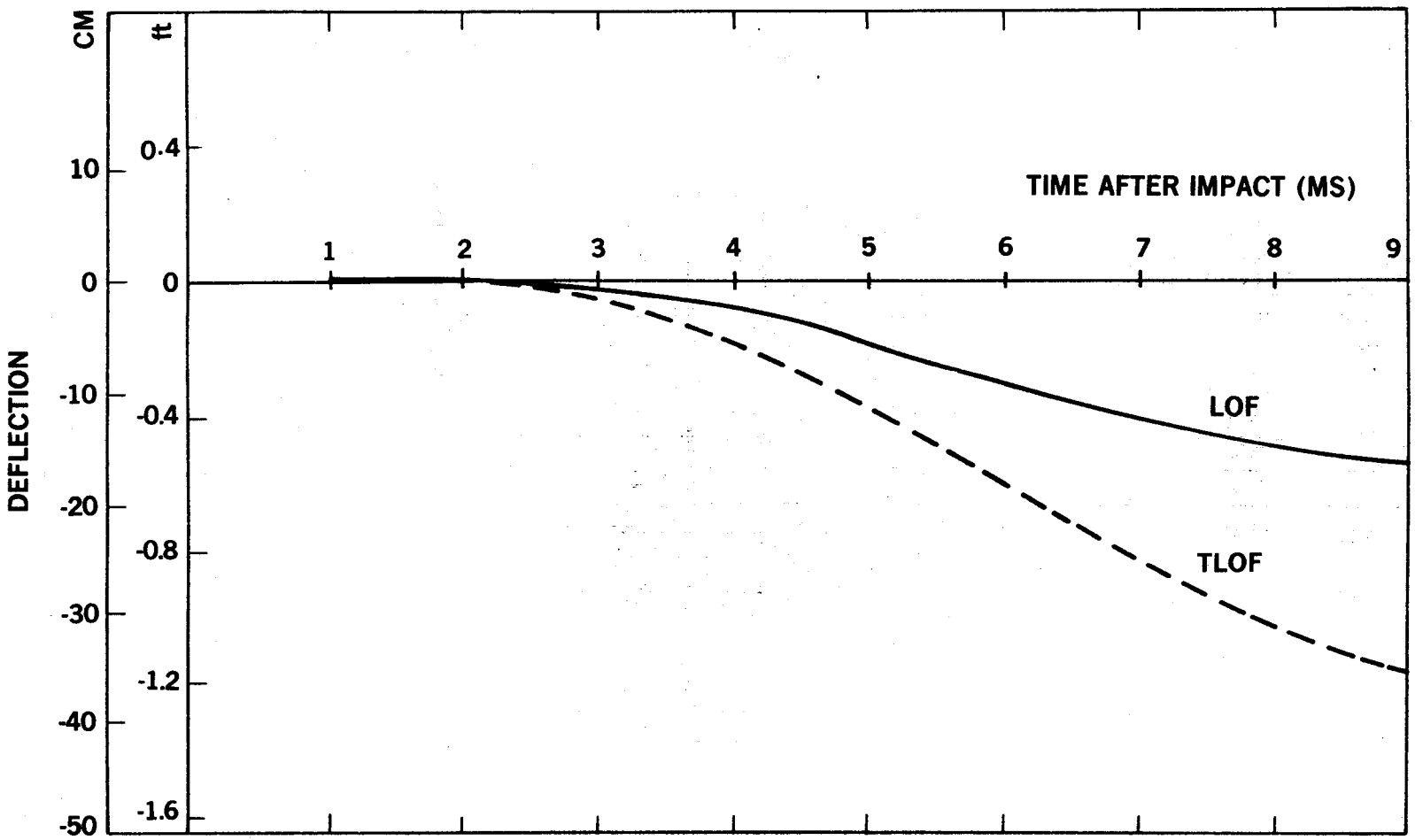

Figure 6. Displacement History of Point D of Figures 4 and 5 Measured Parallel to the Missile Line of Flight (LOF) and Transverse to This Direction (TLOF).

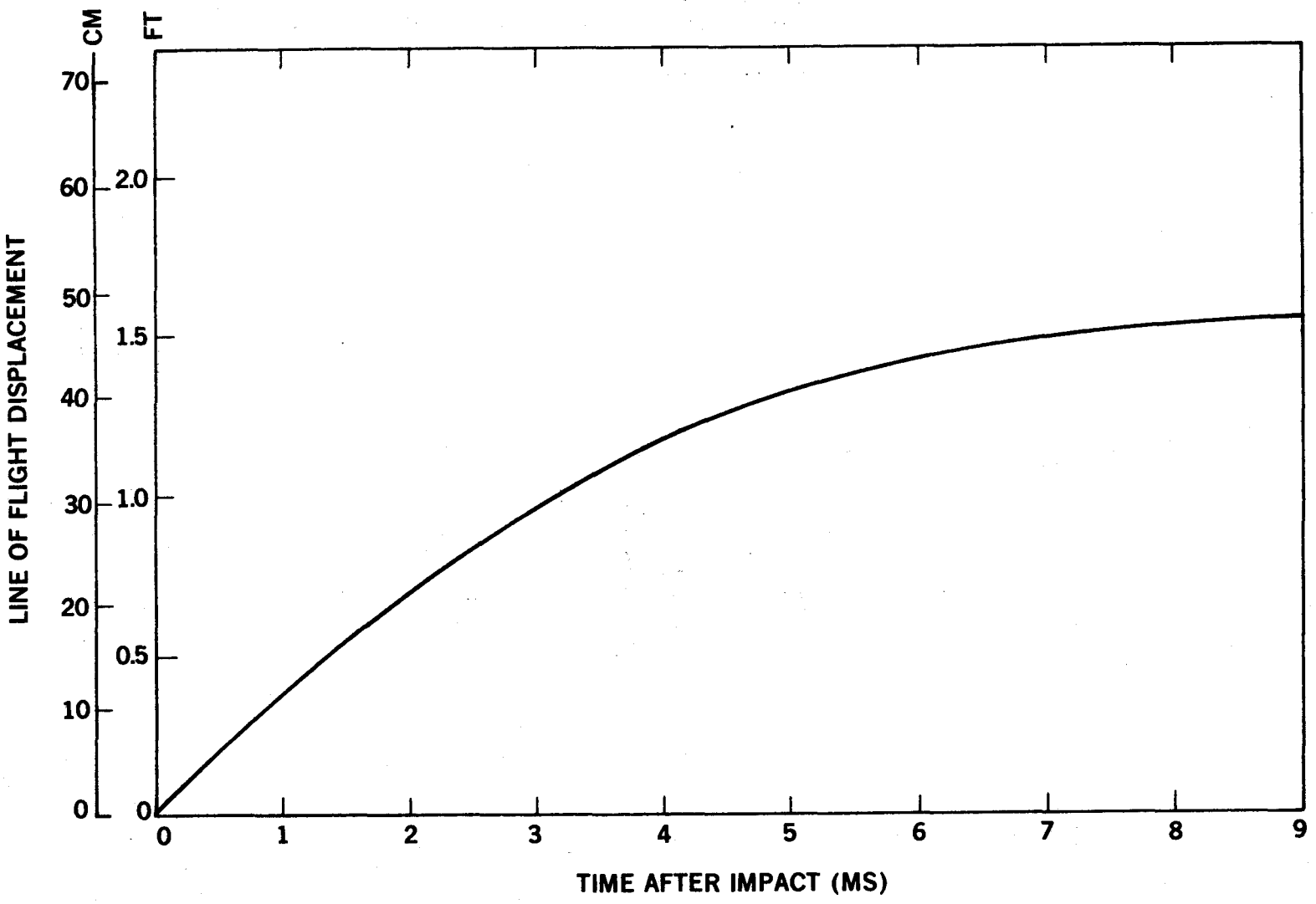

Figure 7. Displacement of Turbine Missile Center of Mass in Line of Flight Direction

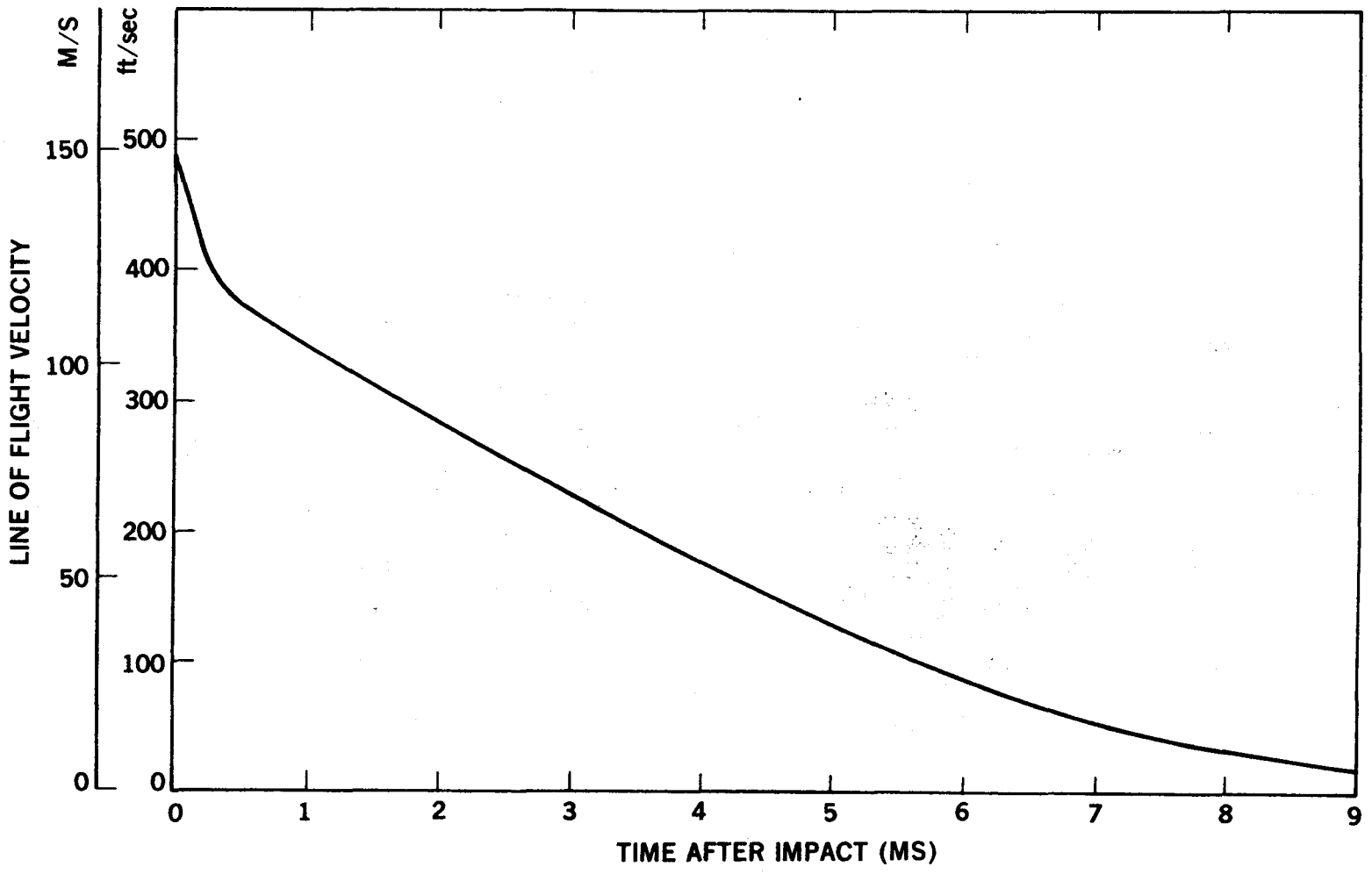

Figure 8. Velocity History of Turbine Missile Center of Mass in Line of Flight Direction

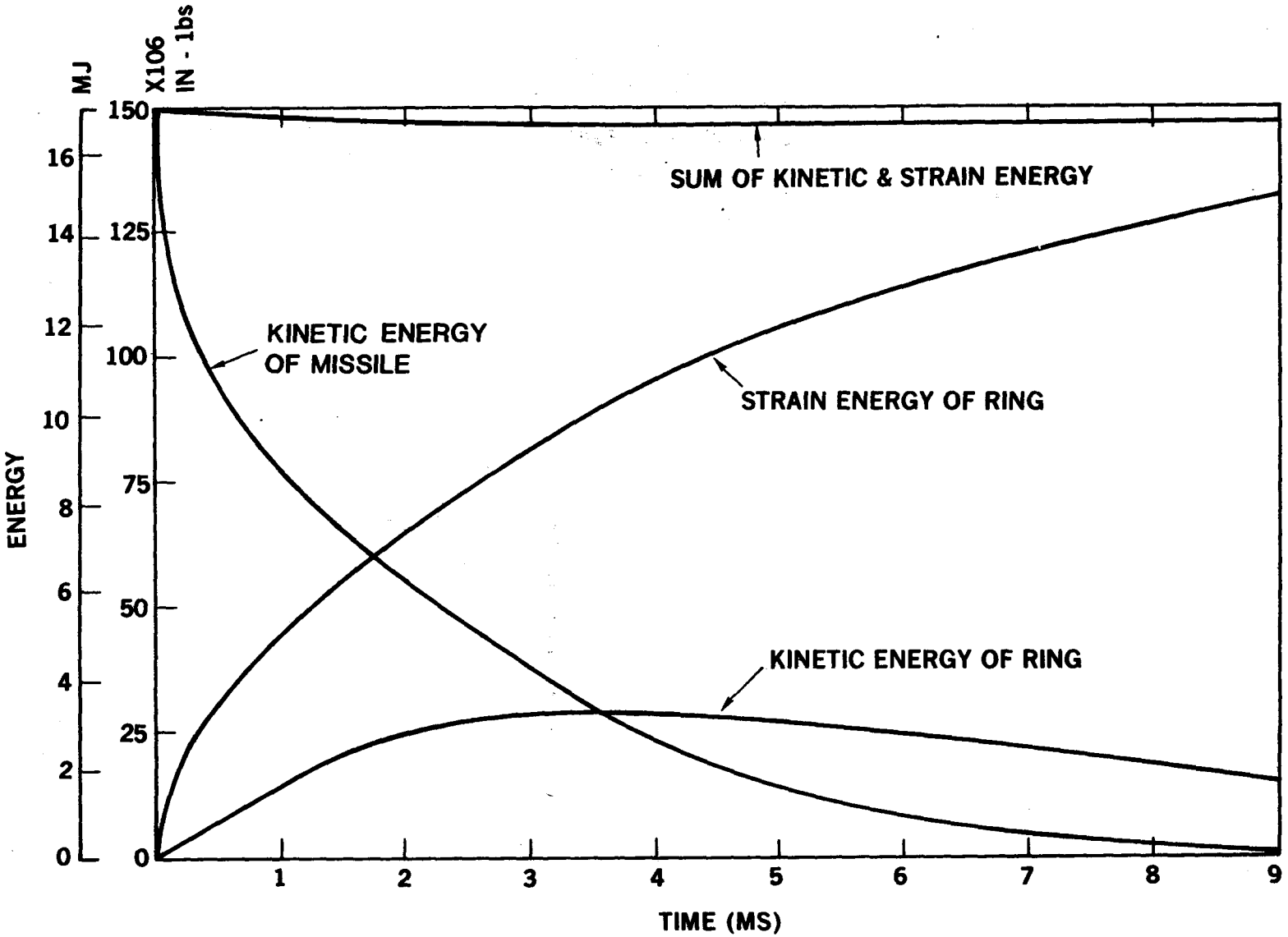

Figure 9. Distribution of Strain and Kinetic Energy During the Course of the Fixed End Rate Dependent Calculation

initial kinetic energy of the missile, which indicates that overall, the calculational results are reasonable. In particular, the sliding interface routine, which is approximate, has not significantly affected the energy balance.

Figure 10 shows the strain-time histories predicted for gages 5, 11, 9. These gages are located immediately adjacent to the right-hand end of the ring with gage 9 on the inner surface, gage 11 at the midsurface, and gage 5 on the outer surface of the ring (see Figure 1). The predominant behavior at this section of the ring is clearly a stretching of the ring although some shear and bending are also present. At late time, the strain levels on all gages are about 4.0%, which implies fully plastic yielding of the ring section. From Figure 3, a 4% strain would correspond to a quasi-static stress level of about 55,000 psi (379 MPa), which implies an axial load in the ring of about 5.5 million pounds (24.5 MN). This is far in excess of the load-carrying capacity of the attachment bolts.

Figure 11 shows the strain-time histories predicted for gages 2, 19 and 7, which were located 36" (0.9m) to the left of the impact point. Gage 2 is located on the outside surface, gage 19 at the center, and gage 7 at the inside surface of the ring. The bending displayed by these records shows that at this location, the ring first straightens out and then at about 5.2 ms, the bending is reversed as the ring tries to conform to the outer radius of the missile

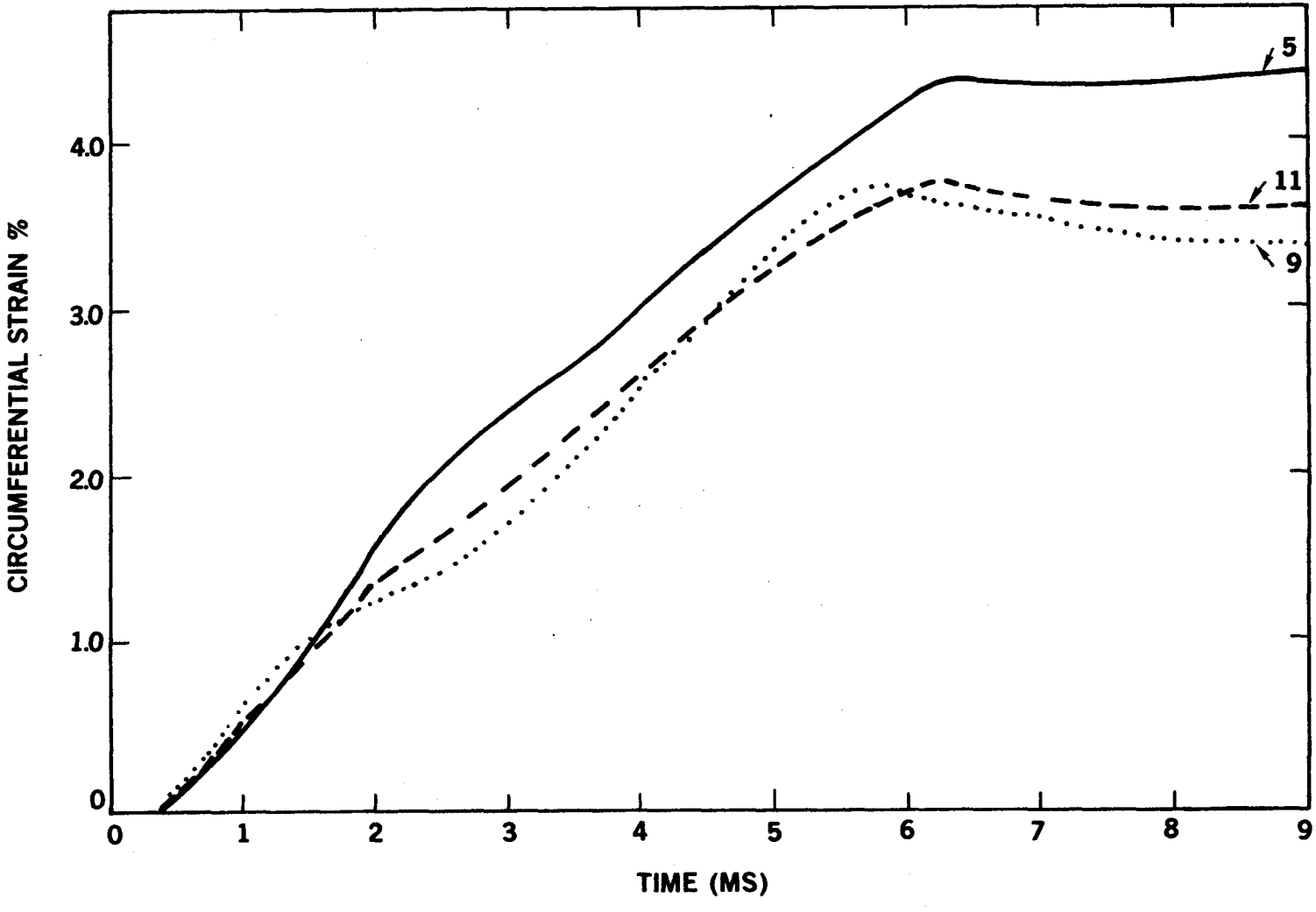

Figure 10. Strain Histories for Gages 5, 11 and 9

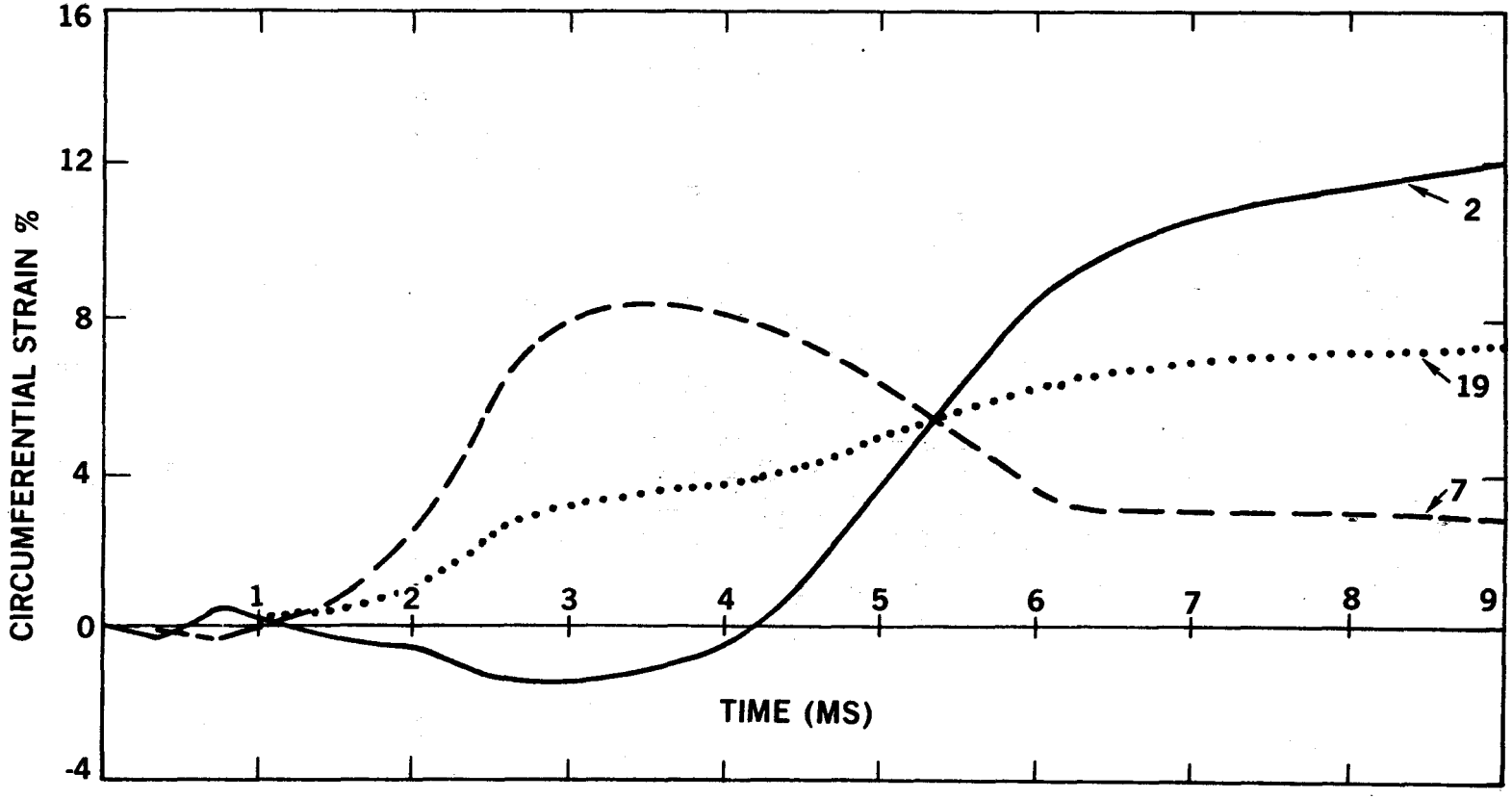

Figure 11. Strain Histories for Gages 2, 19 and 7

segment. At late times, the average strain (gage 19) is about 7%, indicating a large tensile membrane load in the ring.

The final set of predicted gage records, for gages 6, 10 and 1, are shown in Figure 12. These gages are located near the left end of the ring with gage 1 on the outer surface, gage 10 at the centerline, and gage 6 on the inner surface of the ring. In general, the strain levels at this station are less than those shown in Figures 10 and 11; however, this is to be expected since these gages are furthest from the point of impact. At late times, these gages show a large amount of bending as the ring tends to bend toward the impact point (see Figure 5).

In general, all the predicted strain levels for the base-line calculation are much greater than experimentally observed and indicate a tensile hoop loading in the ring which is much larger than the attachment bolts could support. In a later section of this report, we present computed strain gage records for a ring whose ends are free to move. These records show strain levels which are more consistent with the observations.

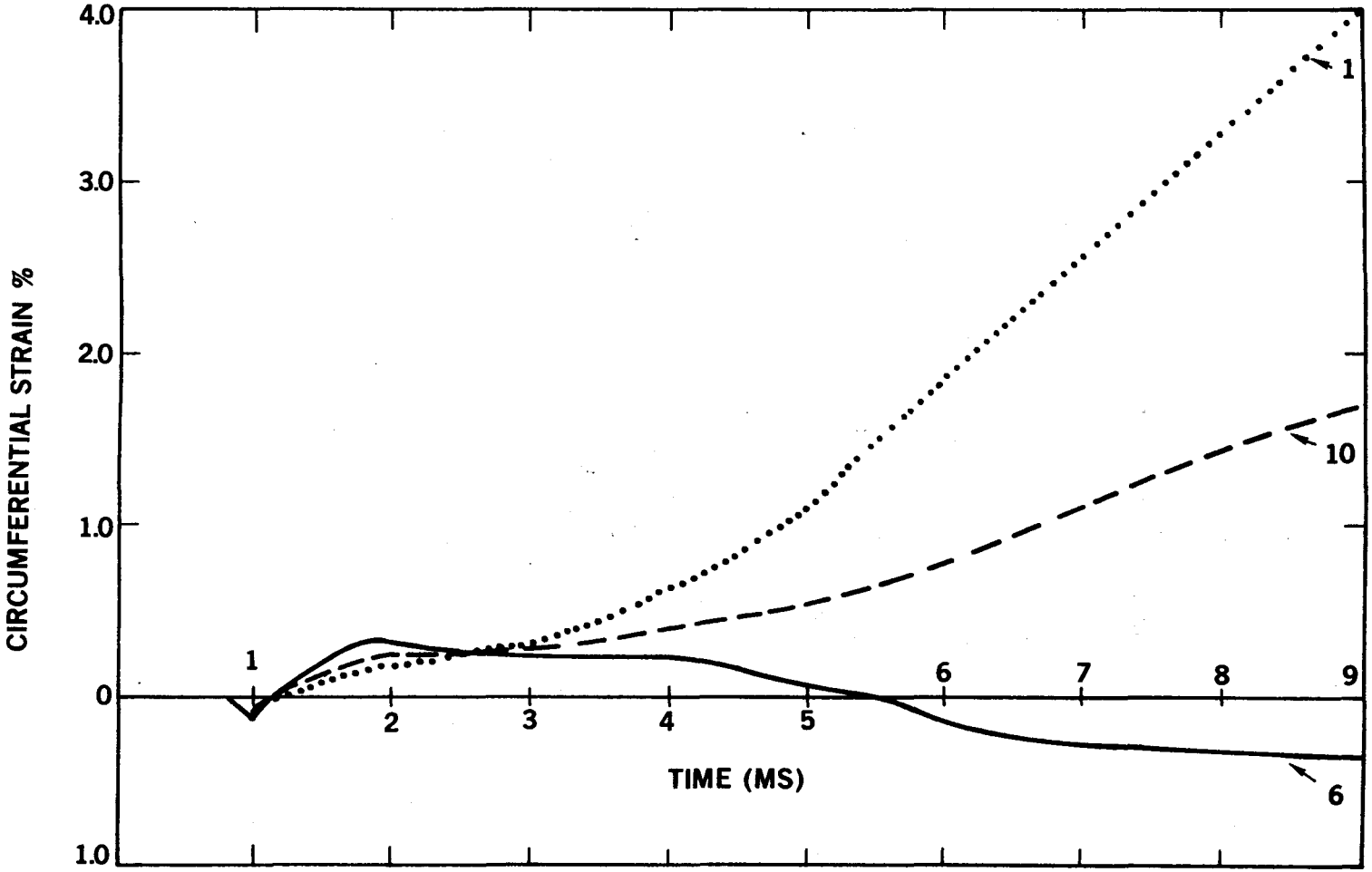

Figure 12. Strain Histories for Gages 1, 10 and 6

IV. Rate-Independent Calculation

The rate dependence assumed in the baseline calculation was typical for that of a mild steel. The high rate test data, obtained as part of this study and discussed more fully in the Appendix, show that at strain rates of 500 s^{-1}, the stress-strain curve predicted by the assumed rate-dependence model is substantially higher than that observed. This would imply that the baseline calculation overestimates the amount of energy absorbed by plastic work. It should be remembered that the average strain rate in the ring during the impact is probably substantially less than 500 s^{-1}. Since at lower strain rates the difference between the stress-strain curves would be smaller, the difference in energy dissipation between the rate-dependent and independent calculation may not be as great as suspected from the results of the high rate tests.

To evaluate the importance of rate dependence in the ring material, a second calculation was performed in which the ring material had the same strain-hardening behavior as the material in the baseline calculation but which was rate independent. Figure 13 shows a comparison between the velocity of the missile's center of mass as predicted by the rate-dependent and independent calculation. In this first millisecond, there are only small differences between the calculations. The rate-independent calculation predicts a slightly greater missile velocity. In the interval of 1 and 6 ms, the difference between the calculations continues to

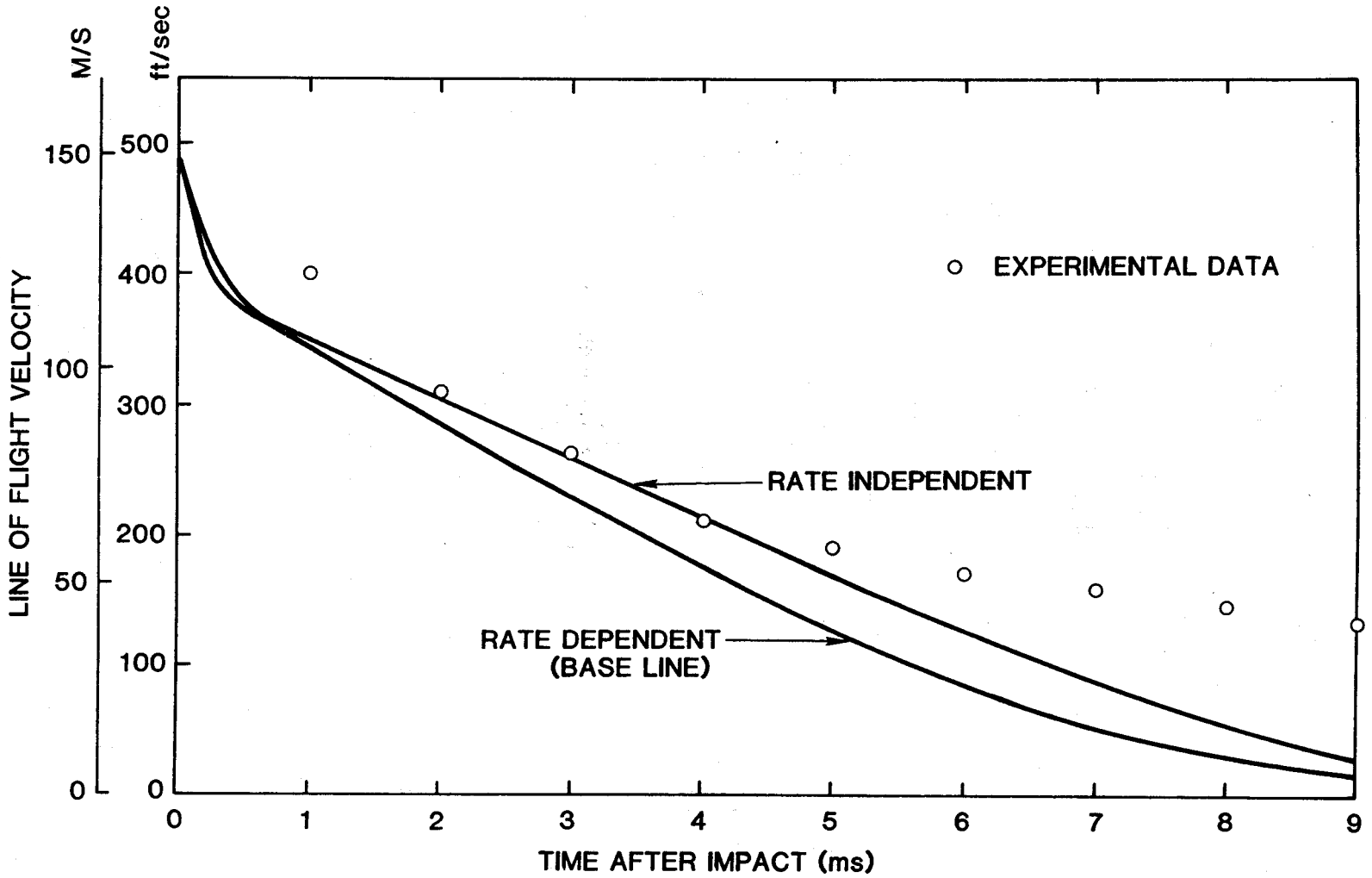

Figure 13. Comparison Between Missile Velocity Histories Predicted by Rate Dependent and Rate Independent Calculations and Experimental Data

grow; however, after 6 ms, the effect of the fixed-ring ends controls the difference between the calculations.

Also shown in this figure are some experimental data points which were obtained from Reference [3]. It is seen that within the interval of 2 to 5 ms after impact, the rate-independent calculation is in excellent agreement with the observed missile velocities. However, for later times, the predicted velocities once again diverge from the observed data due to the fixed-end restraints which are imposed on the ring.

V. Calculation for Ring Having Free-Ring Ends

In the experiment, each end of the ring was welded to a 30"(0.76m)-high, 18" (0.46m)-wide, 5"(12.7cm)-thick flange (Figure 1a). The connection was further reinforced by welding eight 2"(5 cm)-thick gusset plates between the ring and the flange. The flange in turn was bolted to a very rigid supporting structure using twelve 1.5"(3.8cm)-diameter grade 8 bolts (Figure 1a).

It is clear from the high-speed motion pictures of the test that these bolts failed quite early in the test. Furthermore, they can be seen flying about at various times, indicating that they did not fail simultaneously. Tensile tests performed on the bolt steel show yield strengths in excess of 145 ksi (999 MPa) and ultimate strengths in excess of 157 ksi (1.0 GPa). Thus, each bolt should be able to carry a tensile load of about 277,000 lbs. (1.2 MN), and if twelve bolts were equally loaded in tension, a total

reaction of about 3.3 million pounds (15.7 MN) could be supported. Clearly, in the actual test, the support reaction was both a force and a moment, and failure would occur at a lower tensile load. In summary, it would be extremely difficult to realistically describe the failure of the bolted connection.

Nevertheless, an attempt was made to incorporate two "fasteners" into each end flange at locations which coincided with the two rows of five bolts in the actual flange. The cross-sectional area and material properties of the fasteners were chosen to apply the same total load on the flange as six bolts. The flanges and gusset plates were meshed up as shown in Figure 2. The density of the flange material was adjusted to account for the difference in height between the flange and the ring. Thus, the mass and rotational inertia of the flanges in the calculations should adequately model that in the actual test. Sliding interfaces were incorporated at lines denoted by C-C and D-D in Figure 2. Opposing the flange across the interface was a steel block which had fixed nodes on its far side.

A successful calculation incorporating the fasteners was never obtained. Their small size relative to the other meshes caused them to determine the running time step. As they were loaded, the time step rapidly decreased and a time step check incorporated in HONDO automatically terminated the calculation. Alternate ways of incorporating the effect of bolts were considered; however, it appeared desirable to

first run the calculation without any fastening or other tensile restraint. The slide lines at the flanges were still incorporated in the calculations, thus compressive forces could still be applied to the flanges, somewhat restraining their rotational freedom.

Figure 14 shows a comparison between the velocity of the missile's center of mass as predicted by the baseline calculation and the calculation with the flanges without fastenings. In both of these calculations, the ring material was treated as rate dependent. Until 2 ms after impact, the missile velocity is identical for both calculations. This is to be expected since it takes time for the effects of the ring-end conditions to be felt by the missile. Between 2 and 9 ms, the free-end calculation predicts missile velocities which are in better agreement with the experimental data points than those of the fixed-end (baseline) calculation. The experimental data points were taken from Reference [3] and were determined by differentiation of displacement data obtained from high-speed motion pictures. The accuracy of these data at early times, where accelerations are large, is certainly less than that at later times. Thus, the agreement between the free-end calculation and the experimental data at late times is both significant and gratifying.

Additional comparisons can be made between the strain gage responses predicted by this free-end calculation and the experimental records. It was found that the strain

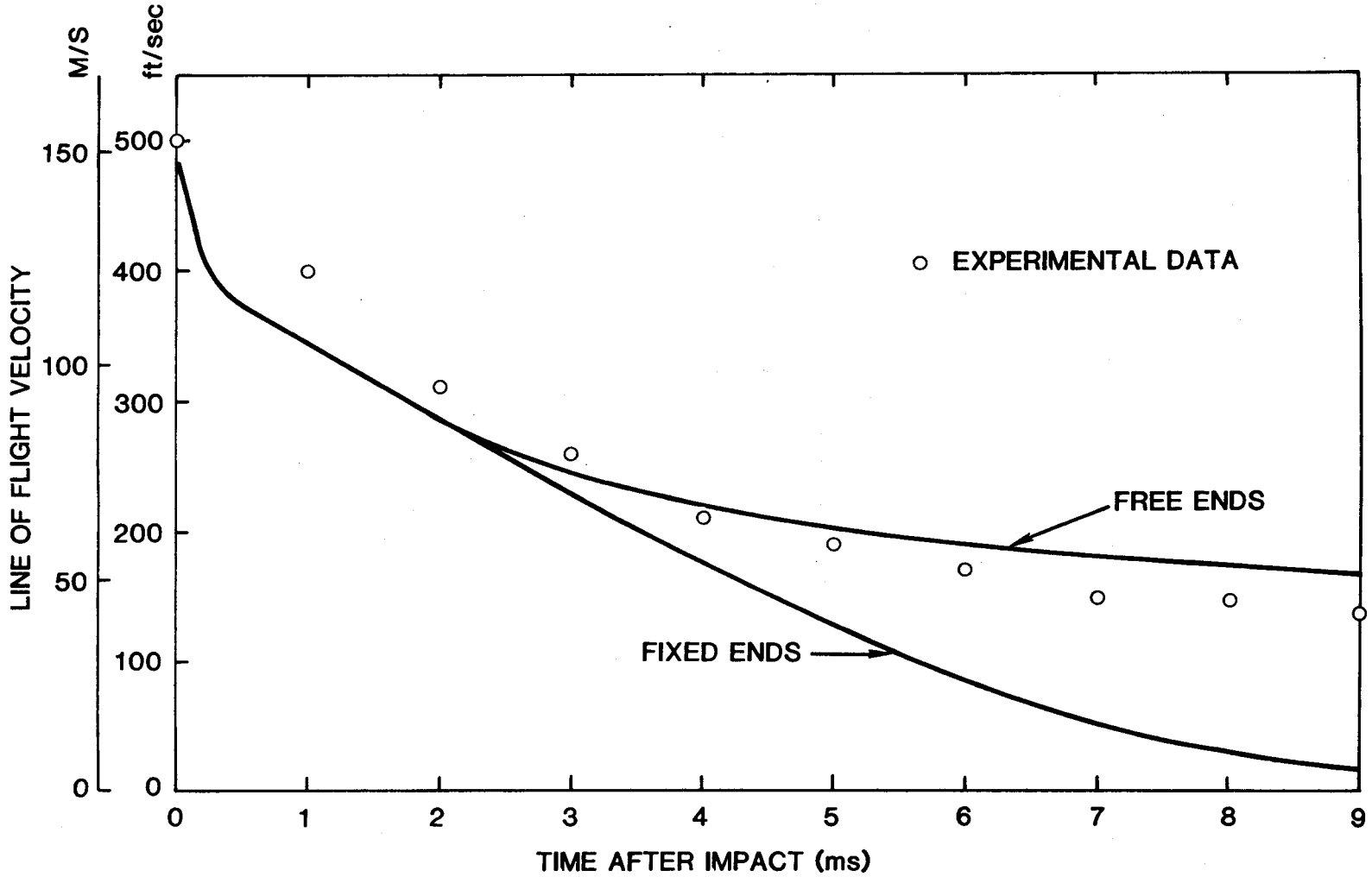

Figure 14. Comparison Between Missile Velocity Histories Predicted by Calculations Having Fixed and Free Ring Ends and Experimental Data

level predicted for gages located at or near the impact point (i.e., gages 2, 3, 4 and 25 as shown in Figure 1) very rapidly exceeded the range of the gage placed on the ring. In all cases, the calculations predicted a signal which went out of range in the proper direction. However, predictions for gages located far from the impact point and near the free ends (i.e., gages 5, 22 and 1 as shown in Figure 1) will be seen to be in reasonable agreement with the experimental records.

Figure 15 compares the predicted and observed response for gages 11 and 13. These gages were located in the middle of the top and bottom surfaces of the ring near the right-hand end of the ring (see Figure 1). The fact that the two experimental records are not identical indicates that the motion of the ring was not two dimensional but included some out-of-plane motion. Nevertheless, both records show a peak of about 1100 microstrain occurring about 2 ms after impact. After this time, both experimental records fall to almost zero at about 3 ms after impact. Between 3 and 5 ms after impact, the differences between the records are most pronounced; however, between 6 and 8 ms after impact, both gages show a fairly constant strain level of 1600 and 1400 microstrain. The calculation predicts a peak of about 1500 microstrain at about .75 ms after impact which is earlier than the experimental record. Except for this time shift in the peak, the early time (< 4ms) agreement between the predicted and observed records is very reasonable.

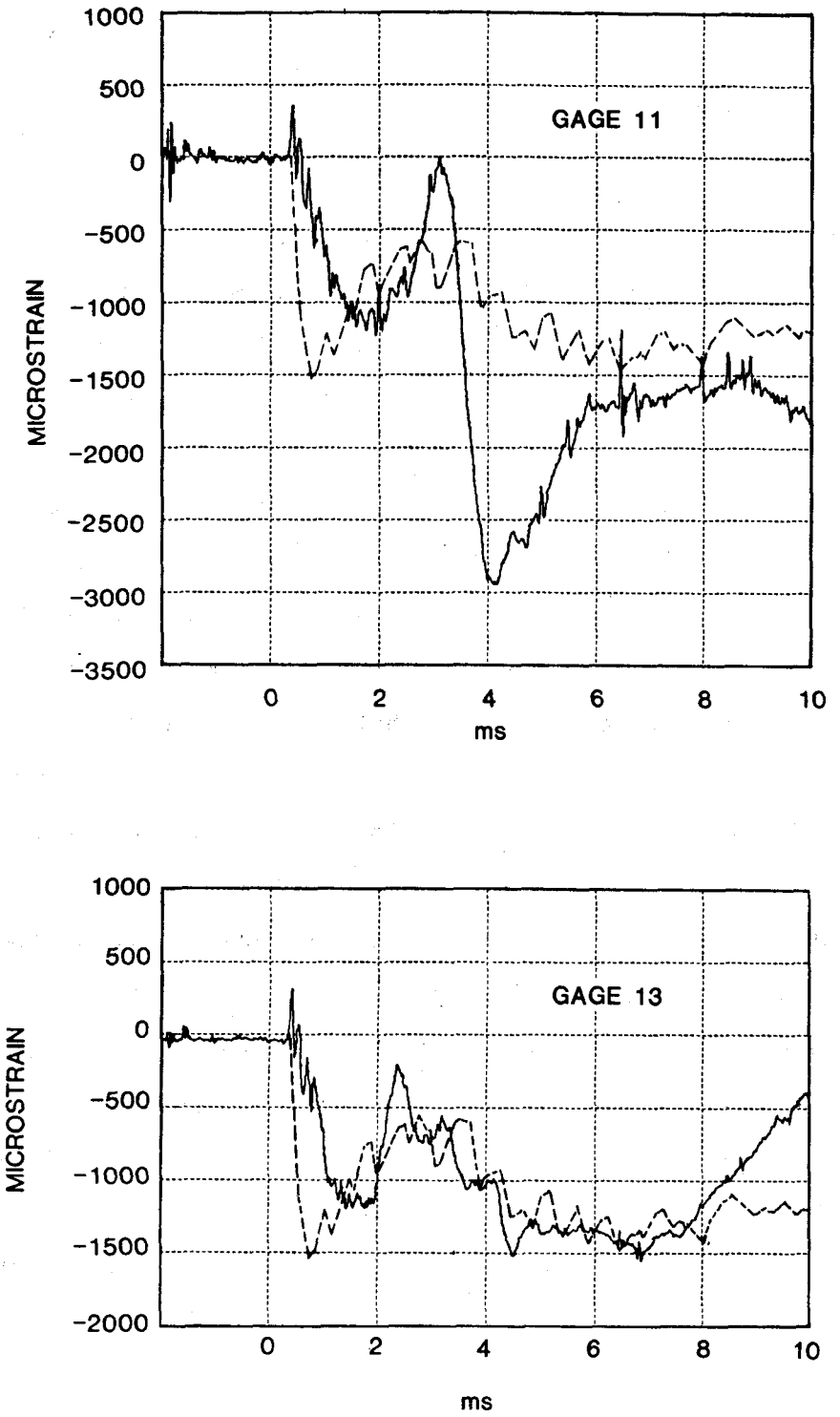

Figure 15. Comparison Between Calculated (Dashed Lines) and Measured (Solid Lines) Strain Histories

Figure 16 shows the comparison for gages 5 and 9. These gages were located at the same station as those of Figure 15 but were on the inner (gage 9) and outer (gage 5) surfaces of the ring. Once again, the calculation approximates the early time ($\leq$ 4 ms) response of these gages but when the strain levels reach about 5000 microstrain (the rated maximum range for the gages), the predictions and gage records diverge.

Figure 17 shows a comparison between the calculated and observed gage records for gages 10 and 12. These gages were located in the middle of the top and bottom surfaces of the ring near the left end (see Figure 1). Comparing the two experimental records, we note that after about 2 ms, there is virtually no correlation between the records, indicating a large out-of-plane motion of the ring at this left end. Before 2 ms, both records show a positive-going spike followed by a slower negative-going signal to about -500 microstrain. This coincidence at early times and discrepancy at late times suggests that failure of the bolts at this end was not simultaneous and was a major contribution to the out-of-plane motion observed at late times. The calculation shows a positive followed by a negative going spike and then a slow decay to a constant level of about 150 microstrain between 6 and 8 ms. This record should probably be compared to an average of the two experimental records.

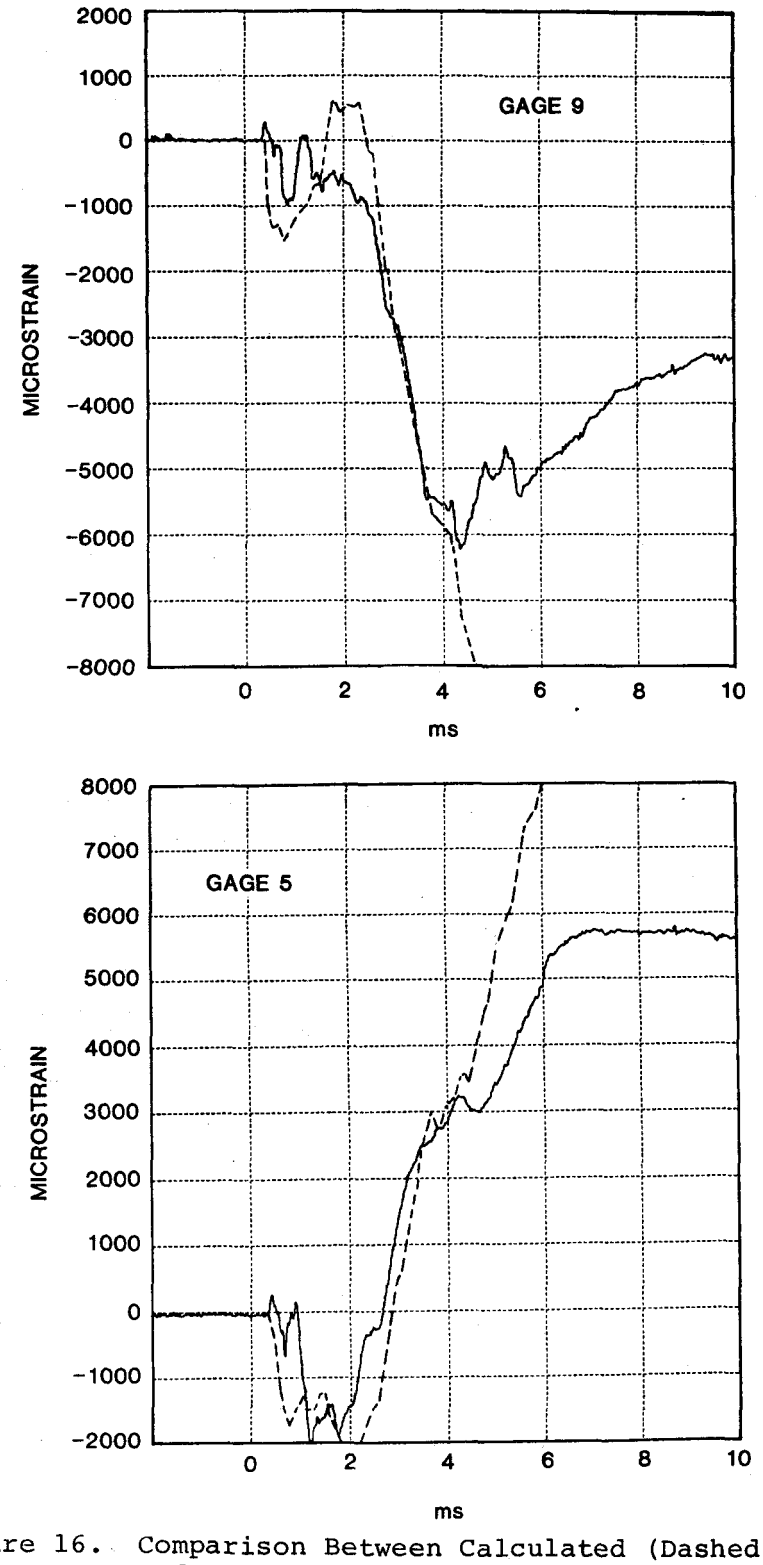

Figure 16. Comparison Between Calculated (Dashed Lines) and Measured (Solid Lines) Strain Histories

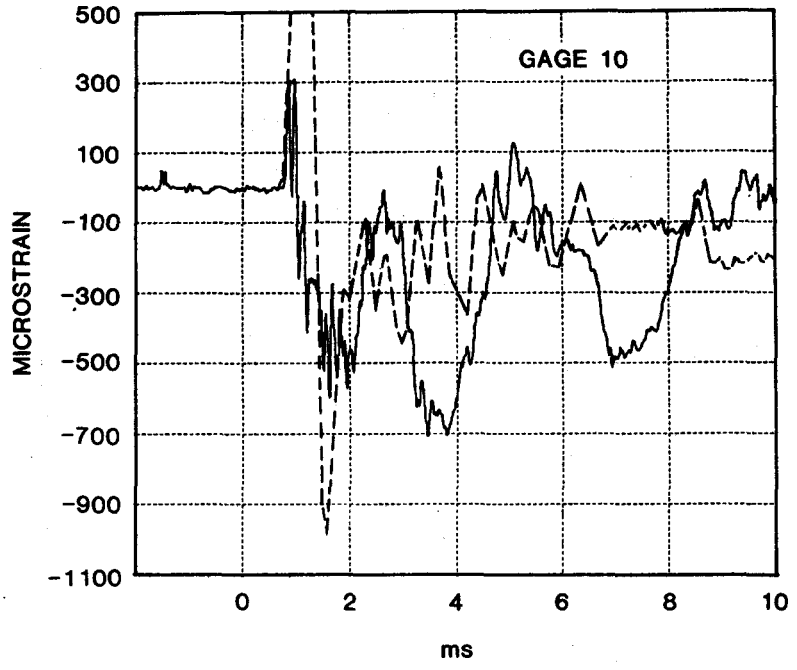

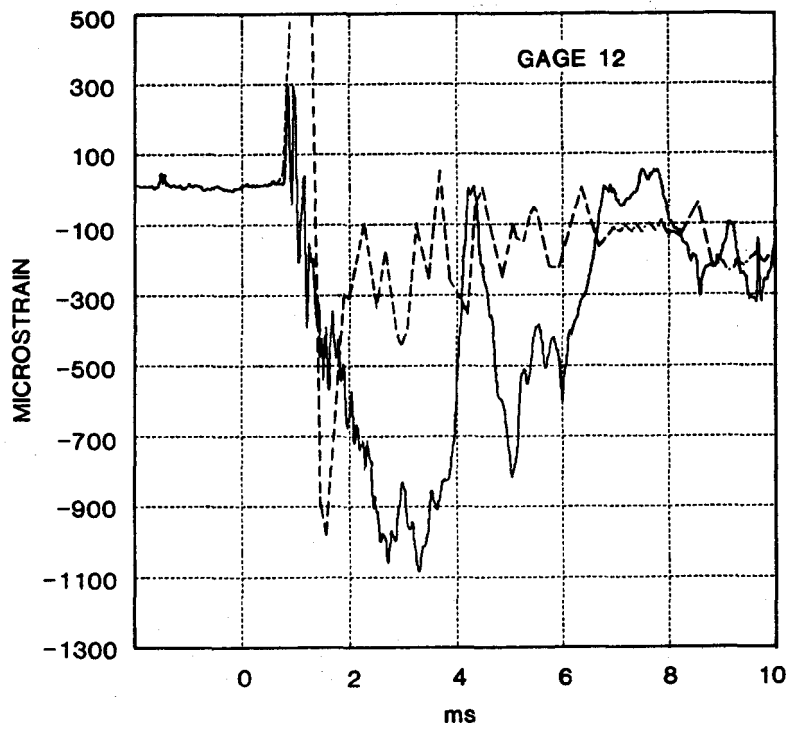

Figure 17. Comparison Between Measured (Solid Lines) and Calculated (Dashed Lines) Strain Histories

Figure 18 shows the comparison between the calculations and gages 1 and 6, which were located on the outside and inside surfaces of the ring at the same station as the gages of Figure 17. For these records, the experimental data and the calculation have comparable magnitudes in early time but there is, in general, poor correlation between them.

Figure 19 shows the comparison for gages 22, which was located on the outer surface of the ring about 53 in. (1.3 m) from the left end (see Figure 1b). The correlation between the calculation and the experimental records is quite good up to strain levels of about 6000 microstrain which is above the rated maximum range of the gage.

Clearly, this free-end calculation provides an excellent representation of the experimental observations. Additional calculations could be performed with changes in material models which reflect the high rate data or the incorporation of the bolts. However, since the experimental data have already demonstrated the effects of non-planar motion, such refinements may not be warranted.

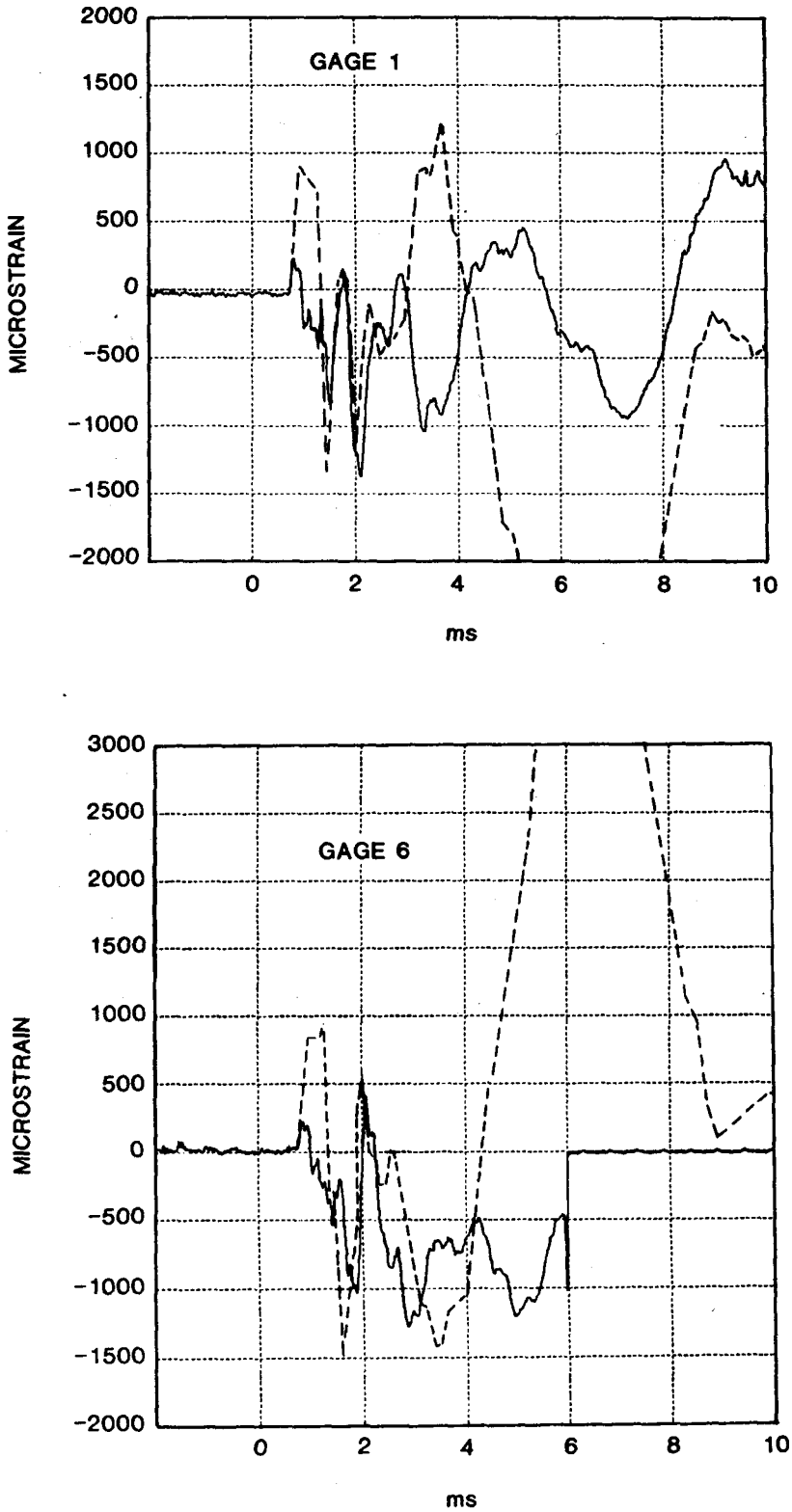

Figure 18. Comparison Between Measured (Solid Lines) and Calculated (Dashed Lines) Strain Histories

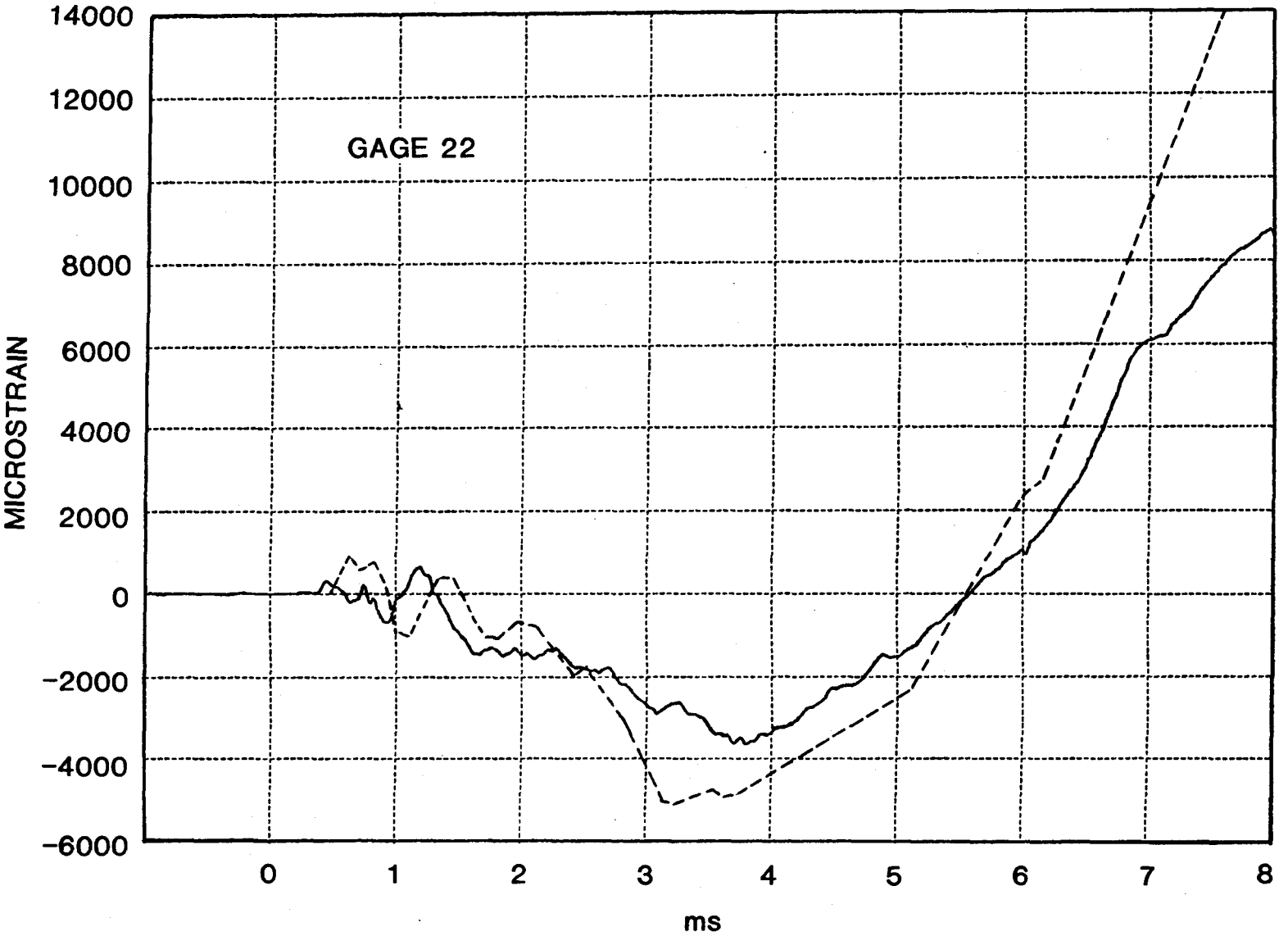

Figure 19. Comparison Between Measured (Solid Lines) and Calculated (Dashed Lines) Strain Histories

VI. Conclusions

1. For structural analysis of accidents involving impact loading, the HONDO code provides an easily usable analysis tool.

2. The baseline calculations assumed an increase in yield strength due to strain rate effects which was greater than that observed in subsequent test of the ring material. However, even with overestimate of rate effects the difference between the rate-dependent and independent calculations was not large.

3. The dynamic response and energy absorbing capability of bolted connections is highly variable and difficult to predict. In computing the ability of structural assemblies to resist impact loads, a straight forward approach appears to perform calculations both with and without fasteners.

4. The calculational results predicted with the free end boundary conditions are in good agreement with both the experimental observations of missile velocity and strain measurements on the ring. Thus in evaluating the energy absorbing characteristics of the structures surrounding rotating machinery a dynamic finite element code, such as HONDO, can provide an alternate to costly experimental testing.

Acknowledgement

I would like to thank Sam Key (5531), developer of the HONDO code, for the valuable discussions and helpful suggestions which he made during the course of this work.

References

1. Protection Against Internally Generated Missiles and their Secondary Effects in Nuclear Power Plants; A Safety Guide, International Atomic Energy Agency, Vienna, 1980.

2. Key, S. W., Z. E. Beisinger, and R. D. Krieg. "HONDO II A Finite Element Computer Program for the Large Deformation Dynamic Response of Axisymmetric Solids," Sandia National Laboratories Report SAND 78-0422, printed October 1978.

3. Yoshimura, H. R., and J. T. Schamaun. "Full Scale Turbine-Missile Casing Tests," Sandia National Laboratories Report SAND79-1505.

4. Gordon, J. T. and J. E. Reaugh, "Strain-Rate Effects on Turbine Missile Casing Impact," Computers and Structures, Volume 13, pp 311-318, 1981.

5. Sliter, G. "Supplementary Information from Casing Test Program, EPRI Memorandum, February 1, 1979.

6. Sliter, G. "Material Properties," EPRI Memorandum, May 1, 1979.

7. Sliter, G. "Request for Summary of Results," EPRI Memorandum, September 12, 1979.

Appendix A

DYNAMIC STRESS-STRAIN DATA FOR A515B Steel

by

L. S. Costin

Division 5532

In order to assess the rate sensitivity of the flow stress of A515B steel, dynamic torsion tests on thin-walled tubes of the material were conducted. All tests were performed using a stored-torque Kolsky (split-Hopkinson) bar. This apparatus is completely described in Reference [1]. With this bar system, a thin-walled tubular specimen is loaded in torsion at a very nearly constant strain rate. By recording the incident, reflected and transmitted waves in the elastic input and output bars, a complete shear stress-shear strain curve can be determined.

All specimens were machined from a 25 mm thick plate of A515B steel. Three sets of two specimens each were machined so that their axes were aligned with one of the three principal directions relative to the rolling direction (L, ST, and LT) (see Fig A1). The specimen tube dimensions were nominally 2.5 mm long, 0.38 mm thick and 10.0 mm in diameter (Fig A1). All tests were conducted so that the nominal strain rate in the specimen was a constant 500 s^{-1}.

Results of these tests are shown in Figures A3 through A7. There appears to be little difference in flow stress or hardening rate between the three orientations. In Figure A8, a comparison of these results with static tensile data ($\dot{\varepsilon} \sim 10^{-4}$ s^{-1}) is shown. The static tensile data were converted to equivalent shear data by assuming a Mises yield condition. Also shown in Figure A8 is the dynamic stress-strain curve derived from the Cowper-Symonds [2] relationship specified for the calculations [e.g., $\tau_o/\tau_s = 1 + (\dot{\lambda}/40)^{1/5}$]. It is evident that this relationship considerably overestimates the dynamic flow stress.

The static and dynamic curves shown in Figure A9 were fitted by a modified Cowper-Symonds relation of the following form:

$$\tau = \tau_y(1+\beta\dot{\lambda})^m\lambda^n \qquad (1)$$

for A515B steel the constants were found to be

τ_y = 320 MPa

$\beta = 10^4 s$

m = 0.02

n = 0.1

These fitted curves are compared to the data in Figure A8. While providing a better fit to the data than the specified rate law, the curves from equation (1) are not adequate at large strains.

References

1. Lipkin, J. and Jones, A. K., 20th U. S. Symposium on Rock Mechanics, Austin, TX, p. 601, 1979.

2. Cowper, G. R. and Symonds, P. S., Tech. Pub. #28, Brown University, Providence, RI, 1957.

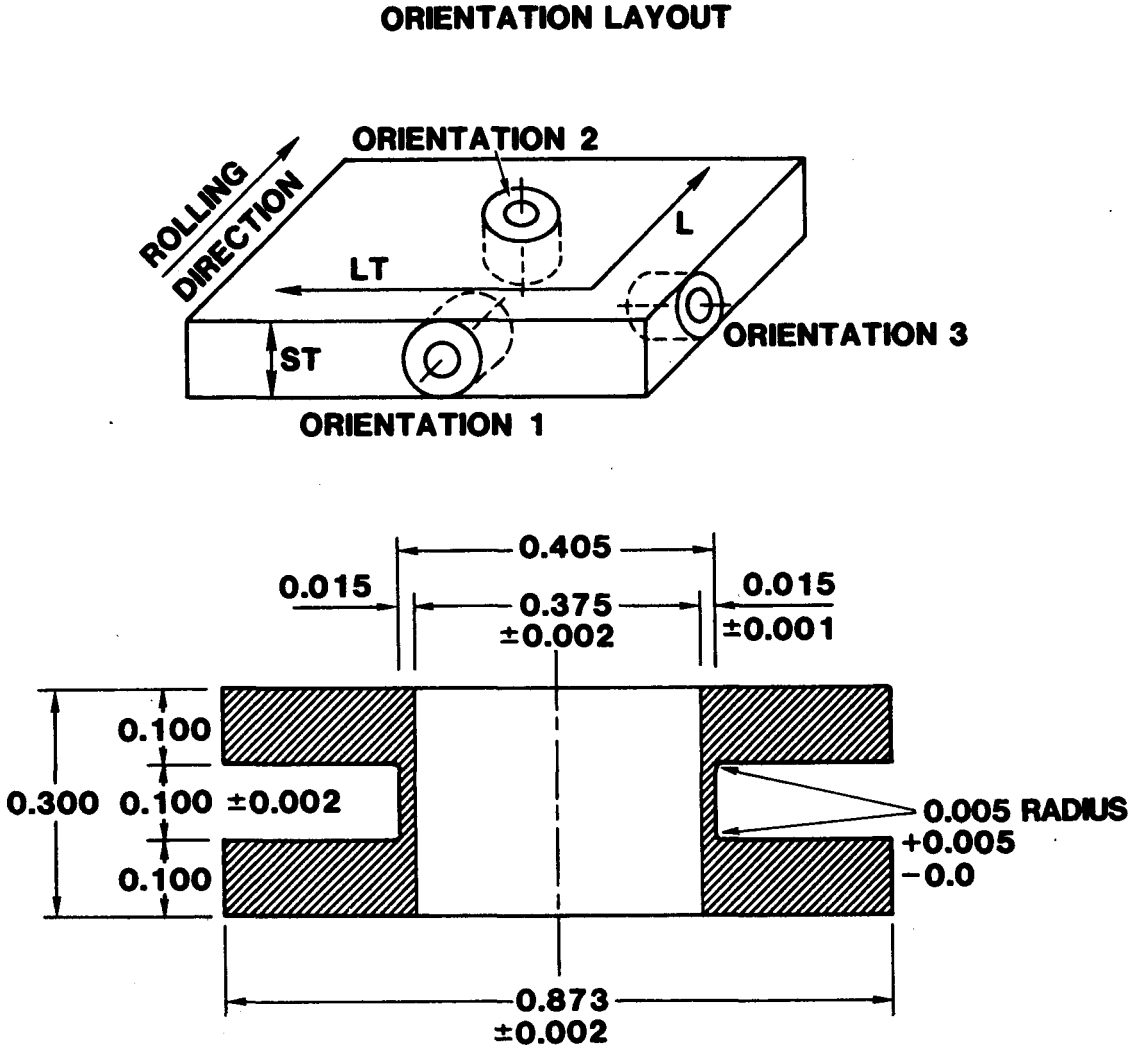

Figure A1. Specimen Details

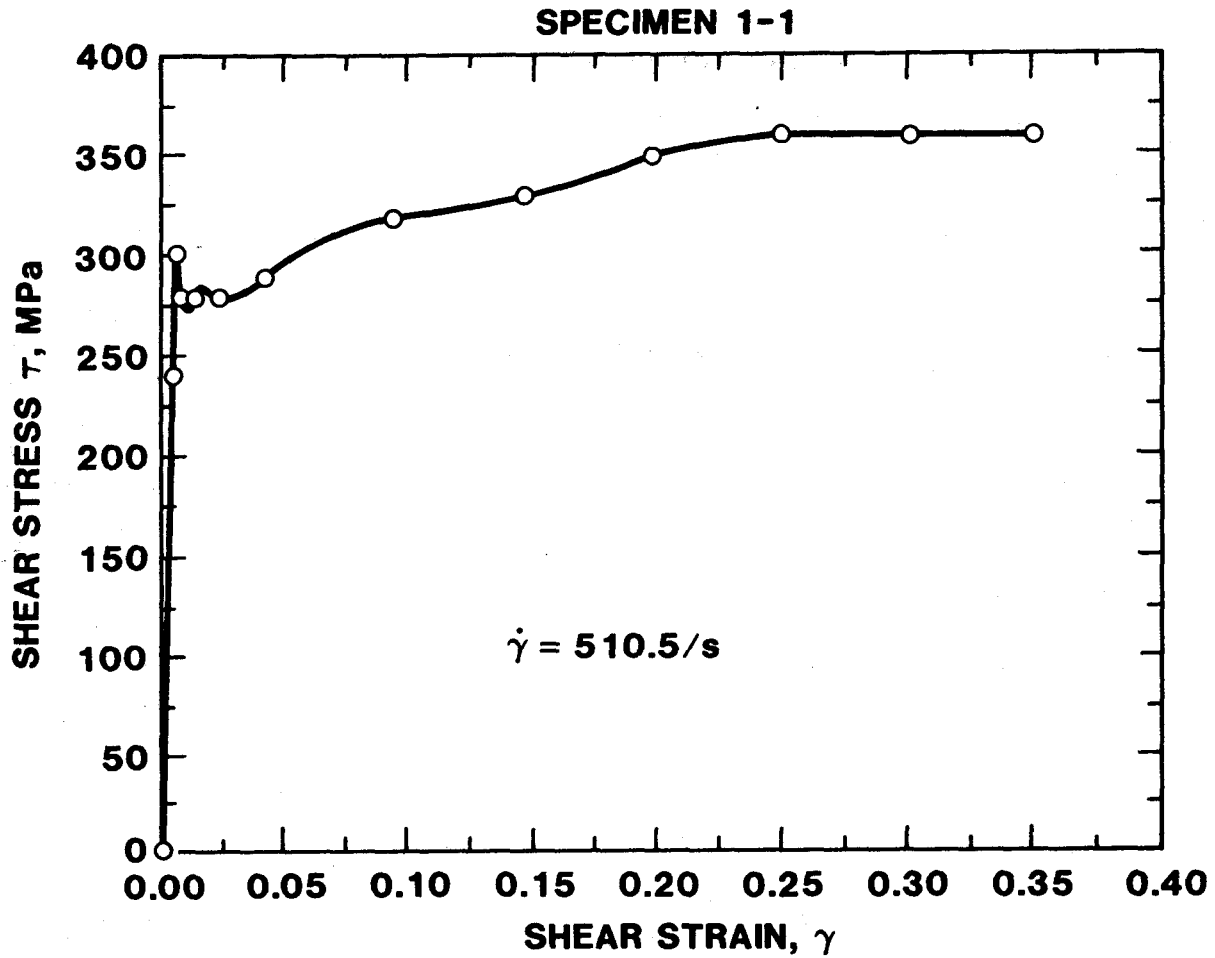

Figure A2. Shear Stress Versus Shear Strain for A515B Steel with Specimen Axis Parallel to the Long Rolling Direction (L)

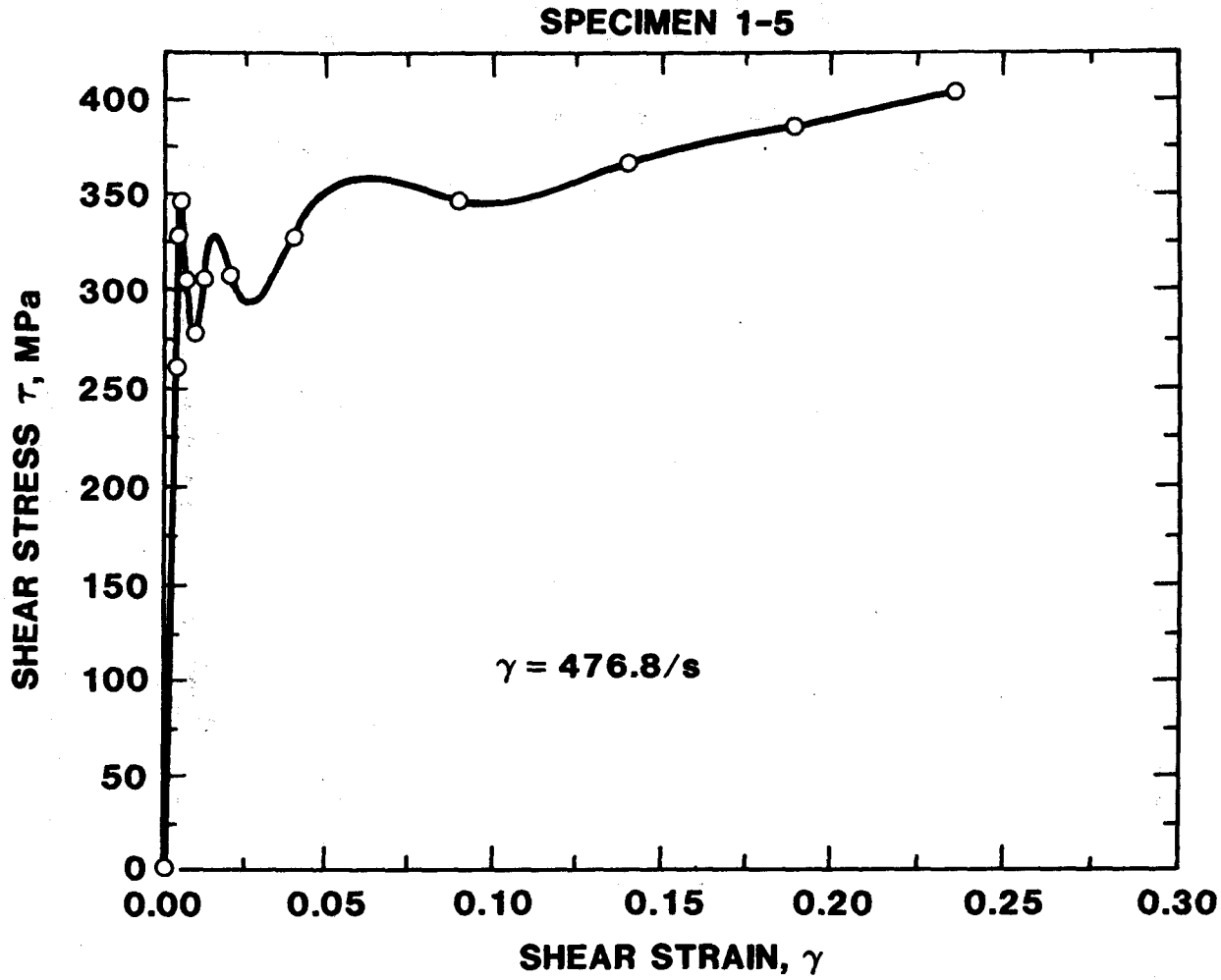

Figure A3. Shear Stress Versus Shear Strain for A515B Steel with Specimen Axis Parallel to the Lcng Rolling Direction (L)

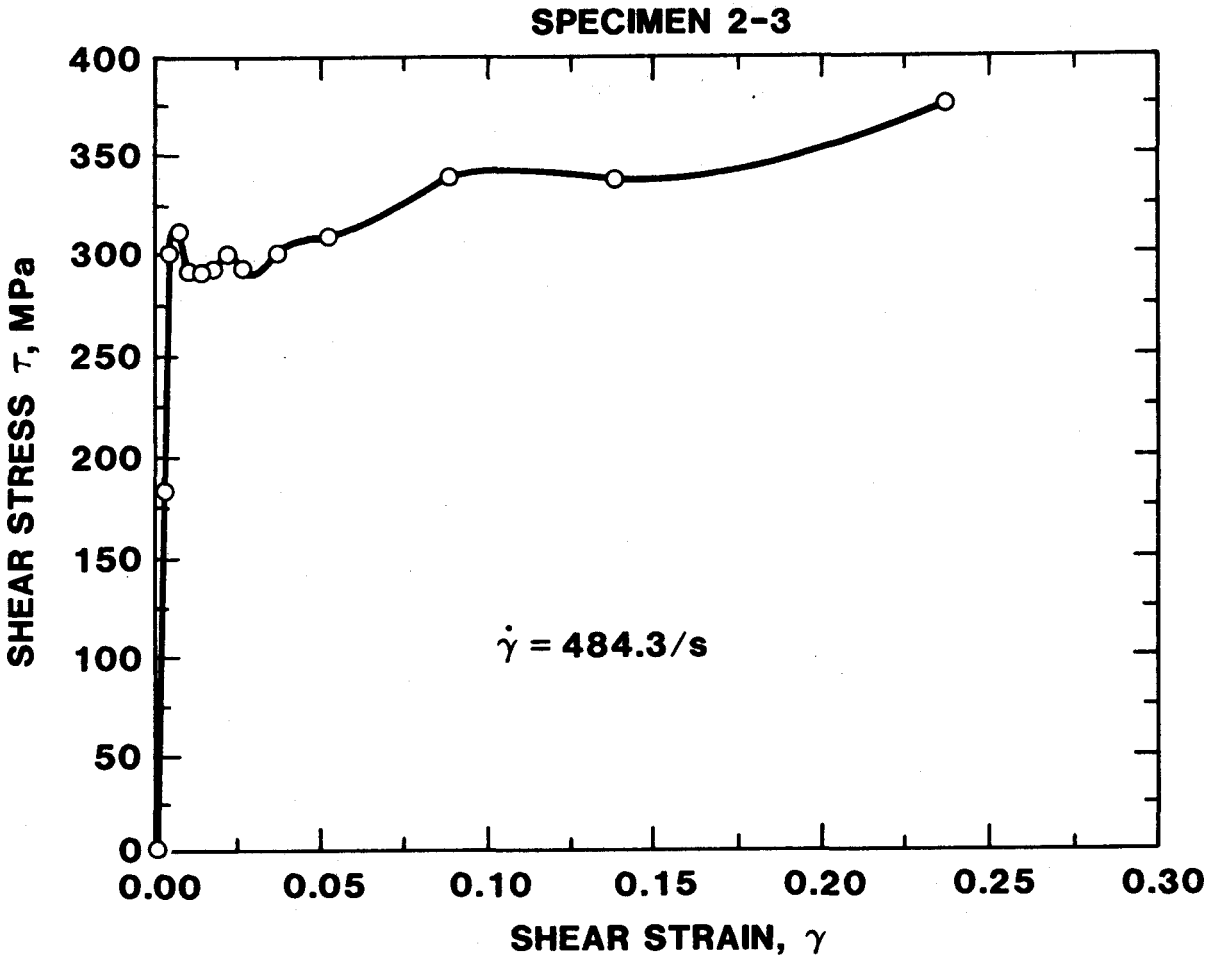

Figure A4. Shear Stress Versus Shear Strain for A515B Steel with Specimen Axis Parallel to the Short Transverse Direction (ST)

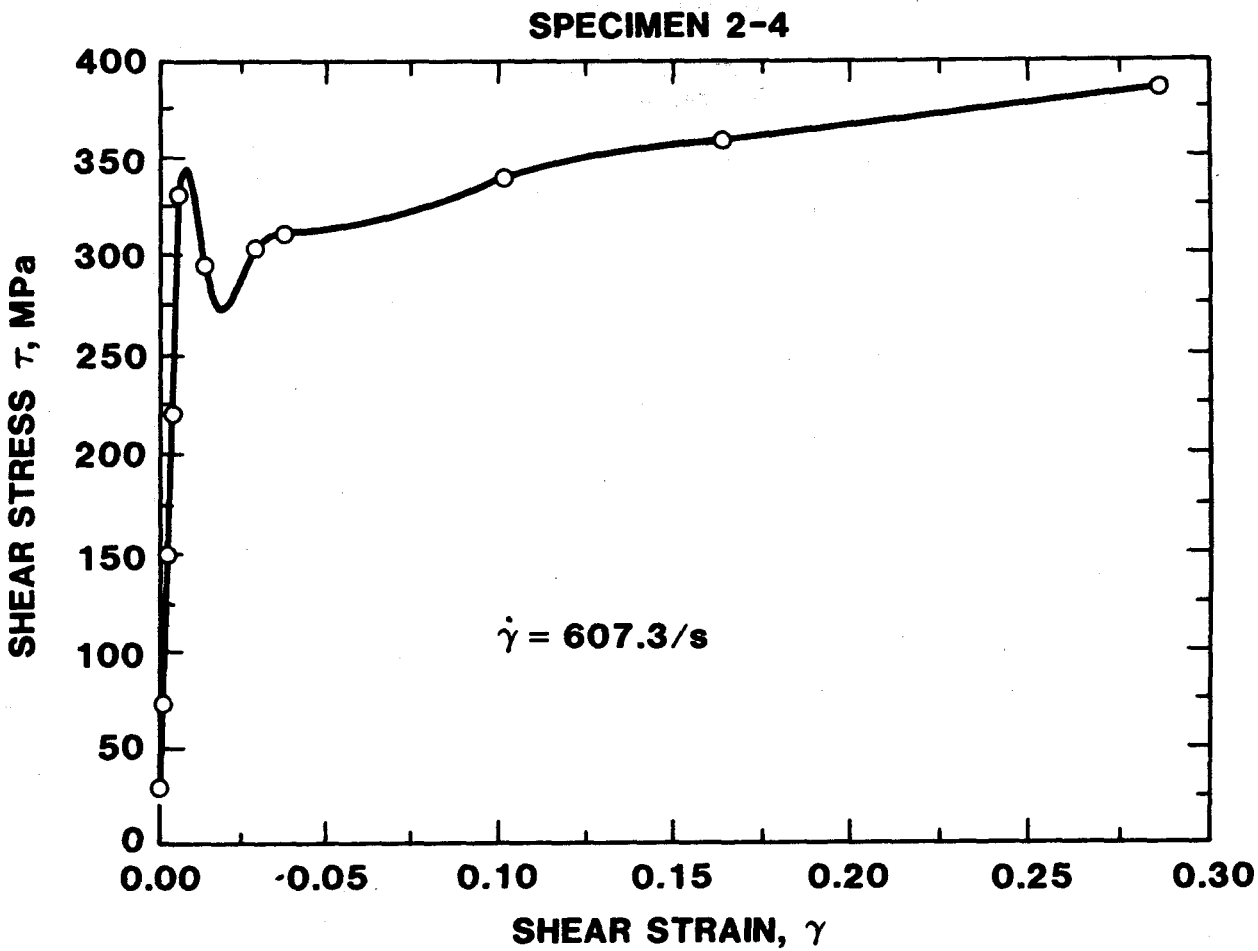

Figure A5. Shear Stress Versus Shear Strain for A515B Steel with Specimen Axis Parallel to the Short Transverse Direction (ST)

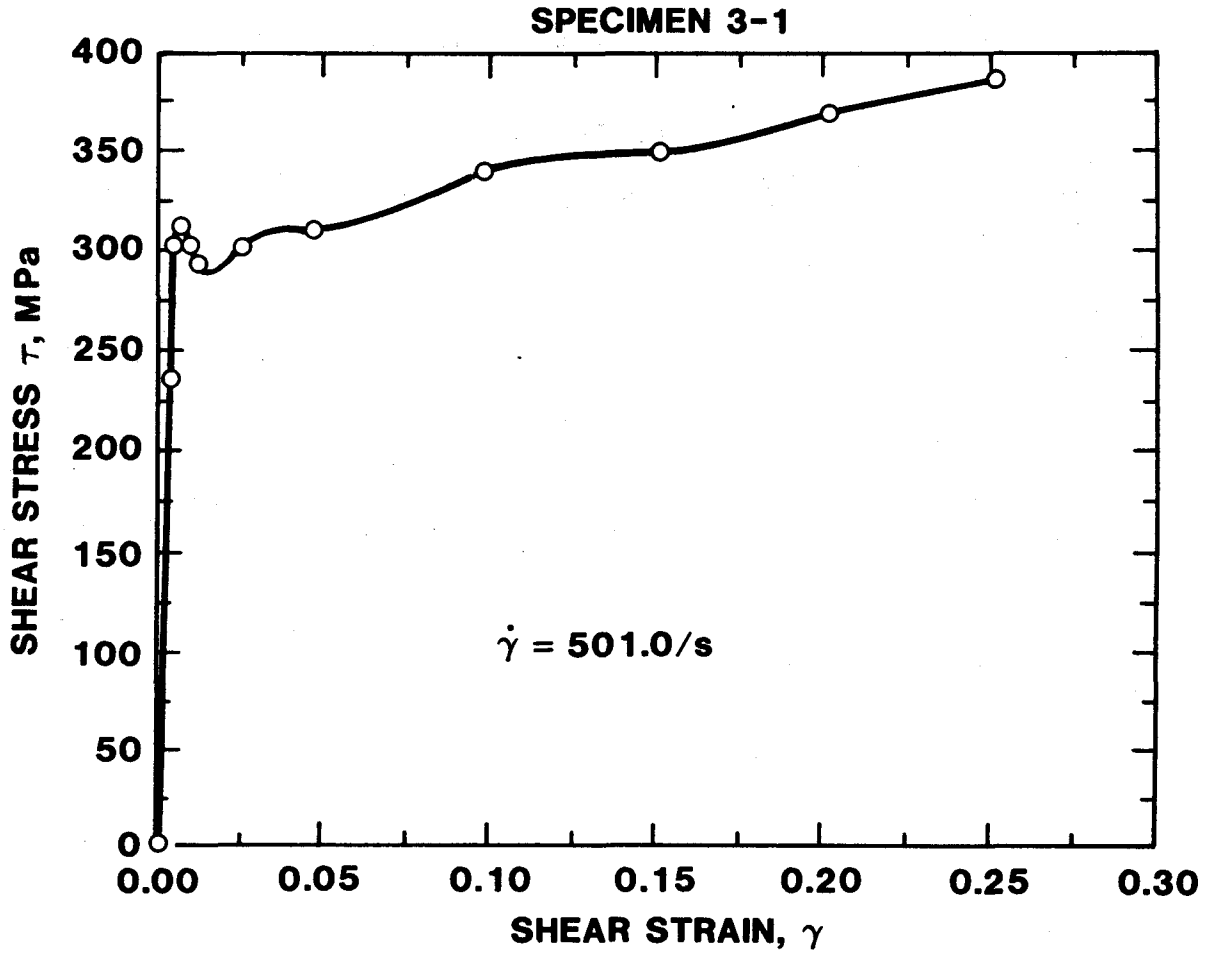

Figure A6. Shear Stress Versus Shear Strain for A515B Steel with Specimen Axis Parallel to the Long Transverse Direction (LT)

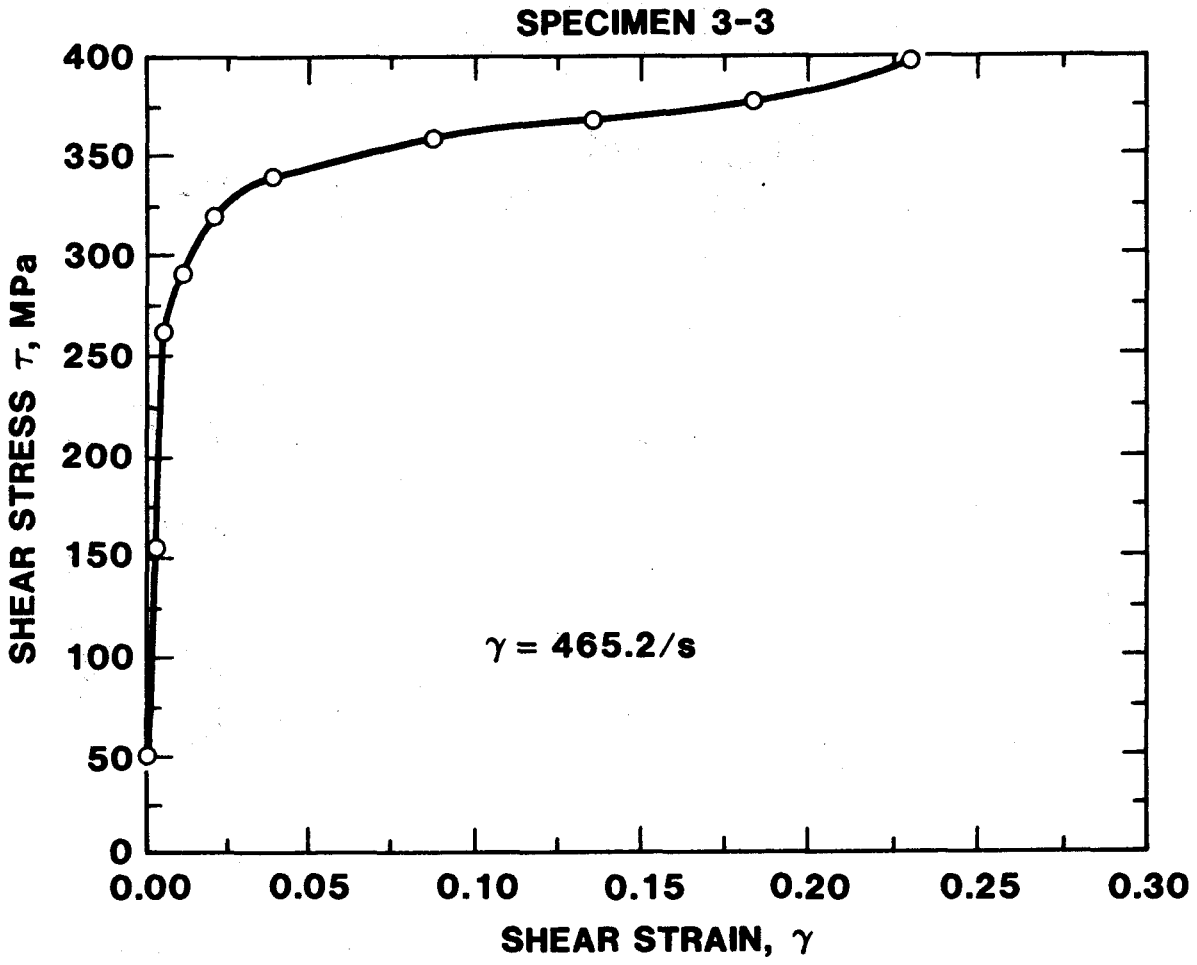

Figure A7. Shear Stress Versus Shear Strain for A515B Steel with Specimen Axis Parallel to the Long Transverse Direction (LT)

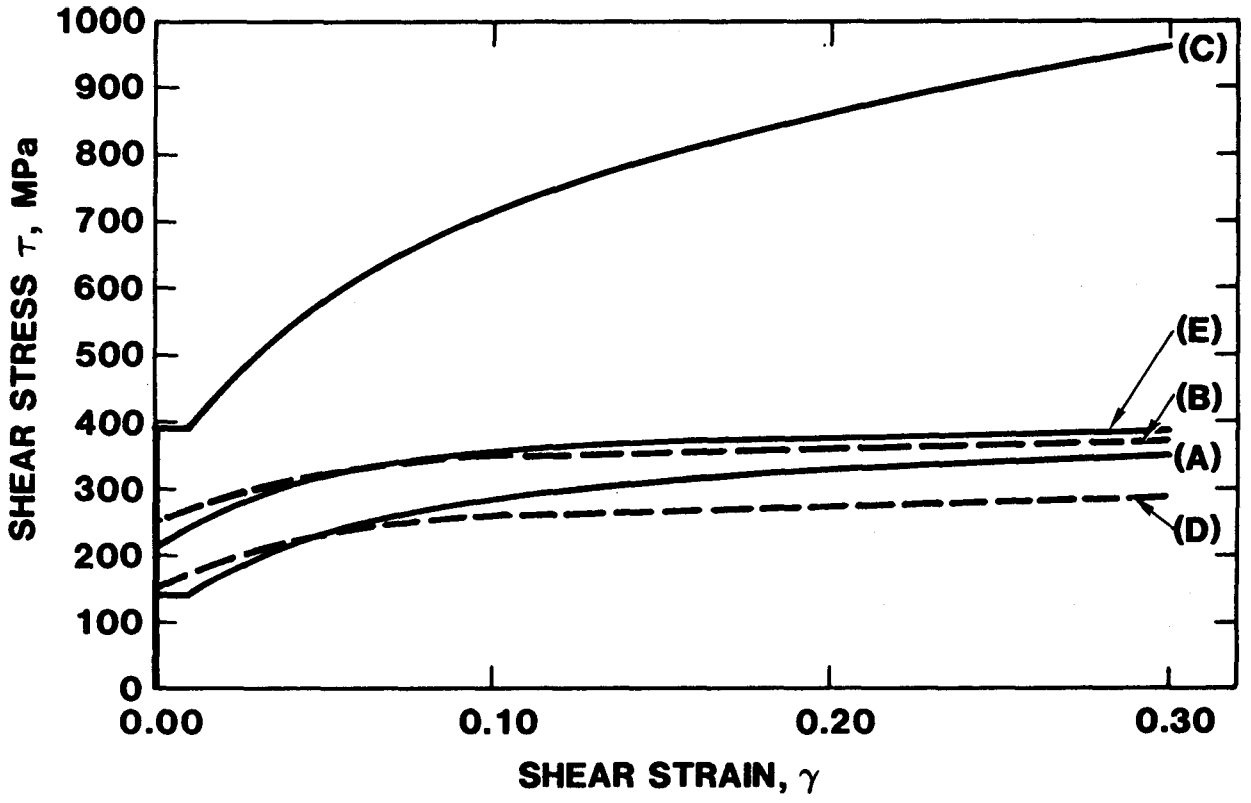

Figure A8. Comparison of Experimental Data to the Proposed Rate Dependent Models. (A) Static Data, (B) Dynamic Data, (C) Cowper-Symonds Relationship Used in Calculations, (D) and (E) Proposed Modified Curves Based on Equation (1), Static and Dynamic, Respectively

Distribution:
Electric Power Research Institute (20)
3412 Hillview Avenue
P. O. Box 10412
Palo Alto, CA 94304
Attn: George Sliter

Northwestern University
Department of Engineering
Technological Institute
Evanston, IL 60201
Attn: T. Belytschko

Massachusetts Institute of technology
Department of Aeronautics and Astronautics
Cambridge, MA 02139
Attn: Emmett A. Witmer

Los Alamos Scientific Laboratory
P. O. Box 1663
Los Alamos, NM 87545
Attn: Paul D. Smith

3141 L. J. Erickson
3151 W. L. Garner (3)
3154-4 C. Dalin (25)
(For DOE/TIC)
4400 A. W. Snyder
4440 G. R. Otey
4442 W. A. Von Riesemann
4442 A. W. Dennis
4442 R. L. Woodfin
4553 H. R. Yoshimura
4747 J. T. Schamaun
5500 O. E. Jones
5510 D. B. Hayes
5520 T. B. Lane
5522 T. G. Priddy
5522 K. W. Schuler (10)
5530 W. Herrmann
5531 S. W. Key (5)
8120 W. E. Alzheimer